

DESIGN OF ELECTRICAL CONTACTS FOR FAST MECHANICAL DISCONNECT SWITCHES

A Dissertation
Presented to
The Academic Faculty

by

Tushar Damle

In Partial Fulfillment
of the Requirements for the Degree
Doctor of Philosophy in the
School of Electrical and Computer Engineering

Georgia Institute of Technology
Dec 2020

COPYRIGHT © 2020 BY TUSHAR DAMLE

DESIGN OF ELECTRICAL CONTACTS FOR FAST MECHANICAL DISCONNECT SWITCHES

Approved by:

Dr. Lukas Graber, Advisor
School of Electrical and Computer
Engineering
Georgia Institute of Technology

Dr. Santiago Grijalva
School of Electrical and Computer
Engineering
Georgia Institute of Technology

Dr. Maryam Saedifard
School of Electrical and Computer
Engineering
Georgia Institute of Technology

Dr. Michael Steurer
Center for Advanced Power Systems
Florida State University

Dr. Michael Varenberg
Woodruff School of Mechanical
Engineering
Georgia Institute of Technology

Date Approved: November 18, 2020

DEDICATED TO

My parents

Ramakrishna Damle
Mohini Damle

ACKNOWLEDGEMENTS

First, I would like to express my sincere gratitude to Professor Lukas Graber, who is one of the nicest professors I have met in my life. His constant encouragement and support to explore new ideas and decide on next steps in research has made me a much better researcher today. I cannot imagine having a better advisor for my PhD.

I would also like to thank Professor Michael Varenberg for always being available to answer any questions I had about tribology and allowing me to use his laboratory equipment. I had to learn about tribology from the scratch during the course of my PhD and the guidance of Professor Varenberg has been invaluable to my research.

My thanks also go to Dr. Michael ‘Mischa’ Steurer and Matthew Bosworth from Florida State University, with whom I have collaborated on multiple projects. Apart from their expertise, working with them has led to me better understanding of the broader area of my research and the projects I would be working on after graduation.

I have worked with a great team of graduate and undergraduate researchers, whose help and input into my research has been invaluable. I would like to thank Prof. Chanyeop Park, Chunmeng Xu and Jia Wei for helping me with various aspects of my research which has led to the completion of my proposal. I would also like to thank Louis Boulanger of the Montgomery Machining Mall for very patiently assisting me with the machining of various parts for my experiments.

Finally, I express my utmost gratitude to my parents, Ramakrishna Damle and Mohini Damle, for their unfailing support and patience throughout my graduate studies. Their

counsel when making important life decisions such as selection of graduate school, transition from Masters' to PhD degree, and their unconditional love has made my graduate student experience a lot easier to navigate. I cannot thank you enough.

TABLE OF CONTENTS

ACKNOWLEDGEMENTS	iv
LIST OF TABLES	viii
LIST OF FIGURES	ix
LIST OF SYMBOLS AND ABBREVIATIONS	xiii
SUMMARY	xiv
CHAPTER 1. PROBLEM STATEMENT	1
CHAPTER 2. STATE OF THE ART	3
CHAPTER 3. RESEARCH OBJECTIVES	19
CHAPTER 4. DESIGN CONSIDERATIONS FOR Piezoelectric FMS	21
4.1 Motivation	21
4.2 Piezoelectric FMS Concept and Operation	22
4.3 Static Simulation Models	24
4.4 Dynamic Simulations	28
4.5 Summary	32
CHAPTER 5. ELECTRICAL CONTACT MATERIAL SELECTION	34
5.1 Motivation	34
5.2 Ashby Method	35
5.3 Material Selection Process	39
5.3.1 Translation Table	39
5.3.2 Derivation of Material Indices	40
5.3.3 Materials Database	47
5.3.4 Material Ranking	48
5.4 Discussion	52
5.5 Summary	54
CHAPTER 6. ELECTRICAL CONTACT GEOMETrY	56
6.1 Motivation	56
6.2 Optimized Contact Geometries	56
6.2.1 Rogowski Geometry	56
6.2.2 Bruce Geometry	57
6.2.3 Chang Geometry	58
6.2.4 Ernst Geometry	59
6.3 Electric Field Analysis	60
6.3.1 Spherical, Elliptical and Flat Geometries	61
6.3.2 Bruce and Rogowski Geometries	62
6.3.3 Ernst and Chang Geometry	64

6.4	Experimental Validation	67
6.4.1	Experiment Setup Description	67
6.4.2	Contact Experiment Results	70
6.5	Summary	71
CHAPTER 7. IMPACT OF FRETTING WEAR		73
7.1	Motivation	73
7.2	Experiment Setup Description	73
7.3	Contact Surface Analysis Experiment	74
7.4	Surface Generation	77
7.5	Electrostatic Field Analysis	79
7.6	Breakdown Voltage Estimation	81
7.7	Summary	84
CHAPTER 8. DISSIMILAR CONTACT MATERIALS		87
8.1	Motivation	87
8.2	Fretting Wear	87
8.2.1	Experiment Description	87
8.2.2	Experiment Results	88
8.3	Thermal Rectification	90
8.3.1	Experiment Description	90
8.3.2	Experiment Results	92
8.3.3	Simulation Model	94
8.3.4	Results	99
8.4	Summary	102
CHAPTER 9. CONCLUSION		104
CHAPTER 10. FUTURE WORK		107
REFERENCES		109

LIST OF TABLES

Table 1 - Comparison OF Piezoelectric FMS TYPES.....	13
Table 2 – Electrical contact material selection approaches for different application	39
Table 3 – Translation Table.....	40
Table 4 – Material Ranking based on each objective	50
Table 5 – Weighted material ranking for case 1	51
Table 6 - Weighted material ranking for case 2.....	51
Table 7 - Weighted material ranking for case 3.....	53
Table 8 - Peak Electric Field of Spherical, Flat and Elliptical Contacts (Radius = 5 mm).....	61
Table 9 - Peak Electric Field of Rogowski Contacts (Radius = 5 mm)	62
Table 10 - Peak Electric Field of Bruce Contacts (Radius = 5 mm).....	64
Table 11 - Peak Electric Field of Chang Contacts (Radius = 5 mm).....	65
Table 12 - Peak Electric Field of Ernst Contacts (Radius = 5 mm)	66
Table 13 – Peak electric field for different contact geometries	66
Table 14 – Surface parameters of the fretting spot above plane level	77
Table 15 - Peak electrostatic field.....	81

LIST OF FIGURES

<p>Figure 1 - HCB commutation methods (a) Counter Voltage [12], (b) Divergent Oscillation [13], (c) Current Injection [14].....</p>	<p>8</p>
<p>Figure 2 - Representation of fault current limitation in AC systems. The fault current is prevented from reaching it’s peak value. [18] [REF].....</p>	<p>9</p>
<p>Figure 3 - Section view of the FMS prototype with all the components– patents pending [49-51].....</p>	<p>13</p>
<p>Figure 4 - Section view of the FMS prototype based on linear piezoelectric actuator.</p>	<p>14</p>
<p>Figure 5 - Design considerations for piezoelectric FMS.....</p>	<p>22</p>
<p>Figure 6 - Amplified Piezoelectric Actuator [72]</p>	<p>23</p>
<p>Figure 7 - Opening and closing mechanism of an amplified piezoelectric actuator in FMS</p>	<p>24</p>
<p>Figure 8 - Actuator Shell Simulation Model.....</p>	<p>25</p>
<p>Figure 9 - Actuator Shell Stroke vs. Force at a thickness of $t = 15$ mm</p>	<p>26</p>
<p>Figure 10 - Actuator Shell Stroke Gain vs Aspect Ratio.....</p>	<p>26</p>
<p>Figure 11- Actuator Shell Stroke vs. Force at a fixed minor axis dimension of $b = 50$ mm.....</p>	<p>27</p>
<p>Figure 12 - Actuator Shell Stroke vs. Thickness at 750 N force.</p>	<p>28</p>
<p>Figure 13 - Stiffness of the actuator shell at different thickness and width</p>	<p>29</p>
<p>Figure 14 - Simscape model of the simplified spring mass system.....</p>	<p>29</p>
<p>Figure 15 - Contact travel curves with different width of actuator shell.....</p>	<p>30</p>

Figure 16 - Contact travel curves with different thickness of actuator shell	31
Figure 17 - Contact travel curves with different mass	32
Figure 18 - Tradeoff plot for minimizing wear damage vs minimizing overheating	47
Figure 19– Rogowski Geometry (left) and Bruce Geometry (right) [60].....	58
Figure 20 – Chang Geometry (left) and Ernst Geometry (right)	59
Figure 21 - Variation of Normalized Electric Field along surface for Spherical, Flat and Elliptical geometries.	62
Figure 22 - Variation of normalized electric field along surface for different Rogowski geometries.	63
Figure 23 - Variation of normalized electric field along surface for different Bruce geometries.	63
Figure 24 - Variation of normalized electric ield along surface for different Chang geometries.	64
Figure 25 - Variation of normalized electric field along the surface for different k values	65
Figure 26 - Variation of normalized electric field along surface for different geometries.	67
Figure 27 - Picture of the Contact Experiment Setup (left); CAD rendering of contact experiment with parts labelled (right).....	68
Figure 28 - Contact bolted to linear motion actuator	69
Figure 29 - CAD model of electrical contact with parts labelled (left); Machined Rogowski contacts ($\phi = 3\pi$) (right).	70
Figure 30 - Contact Resistance vs Force for different contact geometries.	71

Figure 31 - Schematic of ball-on-flat reciprocating tribometer (left) [104], picture of the experiment with a protruding stainless steel flat sample and parts labelled (right)	74
Figure 32 - Optical profile of copper plate after fretting at a) 0.18 A, b) 15 A, c) 30 A, d) 50 A	76
Figure 33 - Electrostatic field between curves representing surfaces separated by 100 μm after fretting wear at 30 A.	80
Figure 34 - Electrostatic field after fretting at the center of contact gap as a function of load current a) with 50 μm gap b) with 100 μm gap.	80
Figure 35 – E-field lines between top and bottom contact surfaces before fretting .	82
Figure 36 – Breakdown voltage vs. fretting current for a) 50 μm b) 100 μm contact gap	84
Figure 37 – R/R_0 during fretting wear (four runs) at 10 A.....	89
Figure 38 - R/R_0 during fretting wear (four runs) at 10 A for different material combinations.....	90
Figure 39 – Thermal Rectification Experiment Components.....	91
Figure 40 – Temperature at of copper-copper and aluminum-aluminum contact pairs with a current of 50 A and 100 A and contact force of 25 N and 100 N... 	92
Figure 41 - Temperature on of copper and aluminum side in Cu-Al contact pairs with a current of 50 A and 100 A and contact force of 25 N and 100 N.	94
Figure 42 – Simulation model showing boundary conditions and temperature measurement locations.	98

Figure 43 – Comparison of simulation and experimental results for Cu-Al contact pairs with a current of 50 A and 100 A and contact force of 25 N and 100 N, respectively.	100
Figure 44 – Relative reduction in temperature on Al side of Al-Cu pair compared to a Cu-Cu pair a) as a function of current at 25 N, b) as a function of applied force at 100 A.....	101
Figure 45 – Relative reduction in temperature on Ag side of Ag-Cu pair compared to a Cu-Cu pair a) as a function of current at 25 N, b) as a function of applied force at 100 A.....	102

LIST OF SYMBOLS AND ABBREVIATIONS

FMS Fast Mechanical Disconnect Switch

HCB Hybrid Circuit breaker

MVDC Medium Voltage Direct Current

HVDC High Voltage Direct Current

APA Amplified Piezoelectric Actuator

MCDM Multi-Criteria Decision Making

MODM Multi-Objective Decision Making

MADM Multi-Attribute Decision Making

CMY Cooper-Mikic-Yovanovich

RTD Resistance Temperature Detector

SUMMARY

The objective of this research is to develop an understanding for the design considerations for electrical contacts with the goal to improve the performance of fast mechanical disconnect switches (FMS). The design of electrical contacts involves tradeoffs between current rating, voltage rating and speed of FMS, which are demonstrated for an FMS prototype based on piezoelectric actuators. The research focus involves the selection of optimal geometries (profile) for the contacts and selection of the most suitable contact material to achieve certain performance goals. Contacts with uniform field geometries such as Bruce and Rogowski were shown to minimize the enhancement of the electric field when open and contact resistance when closed. The most suitable contact materials are identified by deriving the material indices that affect performance of FMS. The material selection process identified minimizing power loss, fretting wear and overheating as the major objectives and copper based contact materials as the most suitable for this application. The impact of fretting wear was further studied and was found to result in a derating of voltage and current rating of FMS. The potential performance gains with dissimilar contact materials are explored. Dissimilar contact materials were found to improve the life expectancy of FMS by delaying the increase in contact resistance caused by fretting wear. The use of dissimilar contact materials to redirect heat away from the temperature sensitive components via thermal rectification is demonstrated through simulation and experiments. The combination of these two effects allow for the design of electrical contacts that can significantly improve the performance of FMS.

CHAPTER 1. PROBLEM STATEMENT

Fast Mechanical Switches (FMS) used in Hybrid Circuit Breakers (HCB) are expected to achieve full contact separation in a sub-millisecond timeframe. This results in FMS having smaller contacts with a contact separation and contact forces at least an order of magnitude lower than conventional circuit breakers. The lower contact separation makes the FMS more susceptible to electrical breakdown due to electric field enhancement caused by the geometry of the contacts. This limits the achievable voltage rating of FMS. The lower contact force increases the contact resistance and makes the FMS more susceptible to wear. The increased contact resistance leads to local heating that deteriorates the contacts, actuators and switching medium and limits the achievable current rating of FMS. Wear also increases the contact resistance over time, which reduces the life expectancy of the FMS. The achievable voltage rating is also reduced due to electric field enhancement around rougher contact surfaces caused as a result of wear.

The stresses experienced by the electrical contacts of (FMS) are different from those of AC and low voltage DC breakers and disconnect switches. The FMS is a non-arcing switch, so prior results on electrical contacts of AC and low voltage DC breakers, which largely focus on deterioration of contacts from arcing, are not fully applicable. The design of electrical contacts can significantly affect the achievable voltage rating, current rating, opening speed, and life expectancy of FMS. This dissertation explores the factors to be considered when designing electrical contacts for FMS. The design factors include the selection of the most suitable materials and geometries for the electrical contacts, the

impact of fretting wear on the voltage rating of FMS and the improvements to the current rating and life expectancy by using dissimilar contact materials.

CHAPTER 2. STATE OF THE ART

2.1 Multi-terminal DC protection challenges

Over the past decade, significant breakthrough in converter technologies has made power distribution by direct current even more promising by providing enhanced reliability and functionality as well as reducing cost and power losses. At the same time, changes in power generation, transmission, and loads such as large-scale integration of renewable energy generation to the power grid, electrification of automobiles, ships and aircraft, as well as increased urbanization, have been the driving forces behind the expansion of high-voltage and medium-voltage power distribution. High voltage direct current grids (HVDC) networks are proposed for power transmission from off-shore wind farms, remote solar farms and connecting asynchronous AC grids [1]. Medium voltage direct current (MVDC) networks are proposed for all electric ships [2], aircraft [3], microgrids [4], electric vehicle charging stations [5], and distribution grids in dense urban regions [6]. Amid the optimism surrounding the benefits of these HVDC and MVDC networks, their protection against DC-side faults remains one of their major technical challenges.

Current HVDC networks are point-to-point transmission lines where DC-side faults are cleared by tripping the power converters on both ends of the lines. To realize the full benefits of HVDC, multi-terminal DC networks are required. A key enabling technology for multi-terminal DC networks are medium and high voltage DC circuit breakers to isolate faulted sections and break short circuit currents. Multi-terminal HVDC networks currently in operation include the three-terminal Nanao 160 kV VSC-HVDC project [7] and the five-

terminal Zhoushan 200 kV HVDC project [8]. Reliable and commercially viable DC circuit breakers are needed for wider adoption of HVDC with more terminals. The protection requirements for MVDC CBs are more demanding than those for HVDC circuit breakers with respect to the fault interruption speed and power density. MVDC networks generally have smaller line reactance than HVDC due to their smaller physical dimensions [9]. Hence, the fault currents in MVDC systems may have higher rates of rise than those in HVDC systems. Thus, MVDC circuit breakers need to clear the fault even faster than HVDC circuit breakers. MVDC circuit breakers installed on electric ships, trains, and aircraft must have compact designs with superior power density and high efficiency. These volume and weight limitations are of lower importance for terrestrial and offshore HVDC circuit breaker installations.

The main challenge in the design of DC circuit breakers is to interrupt the DC short circuit current within a few milliseconds or less. The minimum required opening speed of DC breakers is determined by the rate of rise of fault current $\frac{dI_f}{dt}$ and the peak withstand current I_f . A high $\frac{dI_f}{dt}$ would force the power distribution equipment to be rated for higher short circuit withstand, which would greatly increase their size and cost. A fast switching circuit breaker can clear the fault before the fault current reaches I_f . $\frac{dI_f}{dt}$ is expected to be highest (worst case scenario) under a stiffer source (lower resistive losses) and bolted fault (low voltage drop at fault location), where it depends only on L_s , in which case

$$\frac{dI_f}{dt} = \frac{V_{dc}}{L_s} \quad (1)$$

where I_f is the magnitude of fault current, V_{dc} is the source voltage and L_s is the inductance of the source. In order to estimate the value of L_s , the main impact of such inductance on normal system operation needs to be considered, which is the transient voltage drop across that inductance during short circuit. This value will be limited to the maximum allowable rate of rise/fall of power dp_r/dt in pu/s. Another quantity required to determine L_s is the allowable sudden voltage drop dv_r when the DC system is exposed to such a high power ramp. If such a voltage drop is small (a well-regulated system), the maximum rate of rise of short circuit current is determined by

$$\frac{dI_f}{dt} = \frac{P_r}{V_r} \times \frac{dp_r}{dt} \times \frac{1}{dv_r} \quad (2)$$

where P_r is the rated power of the DC system, V_r is the rated voltage of the system and dv_r is the voltage drop during fault as a fraction of V_r . A breaker with a fast opening time can not only significantly reduce the peak fault current level, but also the amount of energy produced by the fault current, which must be absorbed by the devices in the system. This is particularly useful in medium voltage DC (MVDC) applications such as all electric ships and aircraft, where power density is very important and reducing the peak fault current can reduce the size of devices. For example, to achieve multi-megawatt MVDC shipboard systems, the rated voltages and currents are expected to be in the order of 12-

24 kV and lower kiloamperes respectively [10]. A breaker rated 12 kV and 2 kA continuous current will have a rated power of

$$P_r = 12 \text{ kV} \times 2 \text{ kA} = 24 \text{ MW} \quad (3)$$

As there are no guiding standards for dp_r/dt in DC systems, we look at AC systems where a resistive load can be ramped up from zero to full power in a quarter cycle of power frequency if connected to an AC source at the zero crossing of AC voltage. Hence, a DC system in which power can rise from zero to full power faster than that can be considered as very stiff. Assuming a relatively low $dv_r = 2.5\%$, and a relatively high $\frac{dp_r}{dt} = 500 \text{ pu/s}$, (from zero to full power in 2 ms with only 2.5% voltage drop across L_s), the rate of rise of fault current will not be higher than

$$\frac{dI_f}{dt} = \frac{24 \text{ MV}}{12 \text{ kV}} \times \frac{500 \text{ pu/s}}{(2.5/100)} = 40 \frac{\text{A}}{\mu\text{s}} \quad (4)$$

If the breaker clears the fault in 1.5 ms, this results in the fault current reaching a peak of

$$I_p = 40 \frac{\text{A}}{\mu\text{s}} \times 1500 \mu\text{s} = 60 \text{ kA} \quad (5)$$

This is comparable to the common value of 63 kA prospective fault current rating in 15 kV class AC breakers [11]. AC circuit breakers are mechanical switches with a pneumatic or spring-loaded actuation that moves the electrical contacts. The electrical contacts are enclosed in a vacuum chamber or a gaseous medium of high dielectric strength such as SF₆. However, these breakers have an opening time of 3-5 cycles of AC current,

which is an order of magnitude slower than the required opening time for MVDC applications. Also, the contacts of AC breakers begin to open at the zero crossing of the fault current waveform. Interrupting a DC fault current with no zero crossing would require faster actuation of contacts or a media with better dielectric strength and better arc quenching. As a result, a completely different circuit breaker design is required to interrupt DC faults. A promising solution for protection of MVDC and HVDC is the hybrid circuit breaker (HCB).

2.2 Hybrid Circuit Breakers

The HCB combines mechanical and solid state switching and offers fast protection at low losses and fault current limitation. Mechanical circuit breakers have comparatively low losses but their operation is slow. Solid-state breakers can interrupt currents within a few tens of microseconds but have high on-state losses. The HCB aims at bypassing the mechanical switch by a solid-state switch to break the fault current. The challenge with such an approach is the commutation of the current from the mechanical switch to the semiconductor path. The mechanism of current commutation transfers the fault current to the solid state switch resulting in near zero current through the mechanical switch. At that time, the mechanical switch can start to open and gain voltage withstand capability.

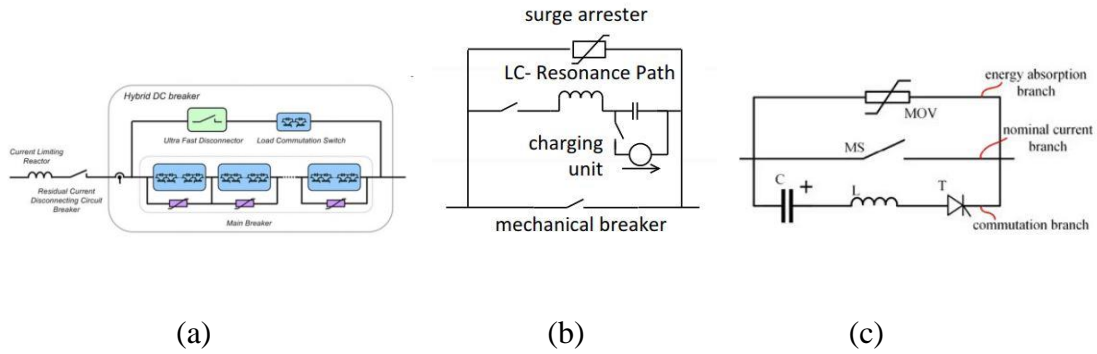


Figure 1 - HCB commutation methods (a) Counter Voltage [12], (b) Divergent Oscillation [13], (c) Current Injection [14]

Zero crossing of current waveform can be artificially induced by one of the following three methods: counter voltage, divergent oscillation and current injection [15]. Figure 1 shows the circuit diagrams of HCB's utilizing each of these commutation methods. In the counter voltage method, a voltage drop is built up to oppose the flow of fault current through the main current path. This is achieved either by the arc drawn by opening a mechanical switch [16], semiconductor switches with turn-off capability [17], superconducting fault current limiters [18], triggered LC circuits [19], or generating a negative voltage in the commutation path. The divergent oscillation method uses a resonant LC circuit between the main and commutation path. During fault, the resonant circuit is excited to produce an oscillatory current, whose superposition with the fault current results in zero current in the main path [20]. The current injection forces the fault current to zero by injecting a current of larger magnitude in the opposite direction. The required energy is stored in a capacitor, which is charged by an external circuit (not shown) [21]. The capacitor can be placed in parallel to the main path [22], in a shunt connection to ground [23] or in the commutation path via inductive coupling [24] and the moment of

current injection controlled either by triggered spark gaps [25] or solid-state switches [26].

The operation of the HCB consists of the following steps:

- When a fault is detected, the fault current is commutated to the solid-state branch via commutation.
- The contacts of the mechanical open when the current flowing through them is zero.
- The solid-state switches will open and break the fault current once after the FMS is open.

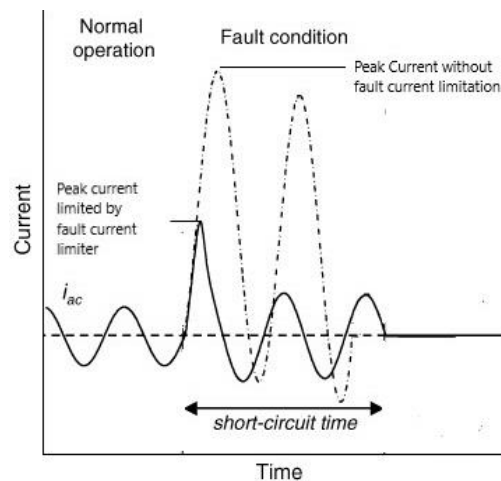


Figure 2 - Representation of fault current limitation in AC systems. The fault current is prevented from reaching its peak value. [18]

HCB's can also act as fault current limiters in AC power grids [18, 27]. The peak fault current in an AC system depends on the X/R ratio of the distribution lines, with higher X/R resulting in higher peak fault current. Lowering the X/R in the lines would lead to increased power losses. The HCB can limit the fault current before it reaches its peak value

in the first cycle, also known as the prospective fault current, as shown in Figure 2. This enables distributed renewable sources such as solar and small scale wind farms to be connected to the distribution grid, which tends to increase nominal and fault current levels in the distribution network [28, 29]. Furthermore, electric utilities in densely populated areas would like to interconnect their distribution substations to increase reliability and resiliency of the grid, as well as add operational flexibility, which would also increase nominal and fault currents. Without fault current limiters, this would require larger and more expansive substations and power equipment to withstand these faults.

The HCB needs a fast-mechanical switch (FMS) to disconnect the main path once current zero is artificially induced. While there is no existing standard, which stipulates the opening speed for this FMS, the consensus is that the switching speed must be less than a few milliseconds [30], which means AC circuit breakers utilizing spring loaded or pneumatic actuators are not fast enough to function as an FMS. Unlike AC circuit breakers, the FMS opens at current zero without the need to break an electric arc. This dissertation focuses on FMS based on piezoelectric actuators and design considerations of electrical contacts for such a FMS.

2.3 Fast Mechanical Disconnect Switch (FMS)

The three variants of FMS that have been built and tested work on the railgun principle [31], Thompson coil [32] and piezoelectric actuators [33, 34] respectively. The Thompson coil is the most common type of FMS in literature and include several variants such as single and double sided coils [35, 36], with air [37] or vacuum [38] as dielectric

medium, built for medium [39] and high voltage applications [40]. All these switches work on the basic principle of electromagnetic repulsion between a moving coil in short circuit and a fixed driving coil that generates rapidly rising magnetic field. Compared to other piezoelectric FMS, the Thompson coil generally has larger displacement (up to 28 mm) [41], high contact forces, and has been built for higher system voltages. However, it also requires more energy to produce the magnetic field and has winding losses and an actuation delay [42].

Piezoelectric actuators typically have a strain of 0.1%, which would require a 1 m long actuator to produce a 1 mm stroke. The piezoelectric FMS in literature use Amplified Piezoelectric Actuators (APAs), which have an elliptical shell around the actuator stack to amplify the strain. A small deformation in the major axis transforms into an amplified deformation in the minor axis. Typical values range from 5 to 20 times of amplification [43]. At the same time, the stiffness is reduced by the same factor and the response time is increased. Other methods to amplify the stroke are variants of the APA concept, such as flextensional [44] and lever arm [45] mechanism. Flextensional mechanism can result in either contraction or expansion of the shell even if the dominant motion of piezo stack is expansion. The lever arm mechanism is a two-step amplification mechanism, which results in up to 40 times greater stroke for the same length of the stack. Both amplified actuator mechanisms produce larger stroke at the cost of opening speed and contact force. The piezoelectric FMS in open literature include a 15 kV, 200 A vacuum switch based on APA with 4 contact pairs in series to achieve contact separation of 0.5 mm [46-48]. Another variant of the piezoelectric switch is a 300 V, 350 A version with a single contact pair. It

can achieve open contact separation around 300 μm , contact force around 40 N, and an opening speed around 0.5 ms [34]. The latter switch operates in air, which results in a lower voltage withstand capability compared to the former vacuum-insulated switch [34, 49]. In general, piezoelectric FMS are faster and have no appreciable energy loss in its driving circuit. However, the contact separation, contact force, and voltage ratings are lower than the Thompson coil [50]. No FMS based on magnetostrictive actuators is currently documented in the open literature.

Figure 3 shows a 15 kV, 200 A FMS prototype based on APA. The FMS has two ceramic bushings that act as electrical and thermal terminals on top of the grounded vacuum chamber. The APA is housed in a polymeric frame to which the outer conductors and the contact tabs are attached. The actuator is controlled by charging and discharging its electrostatic capacitance. The control wires pass through a multi-pin feedthrough so that they can be interfaced from outside the vacuum chamber. Moving contact tabs made of Sterling silver ($\text{Ag}_{92.5}\text{Cu}_{7.5}$) are attached to the polymeric frame. The FMS consists of four identical contact pairs with hemispherical contacts of 5 mm diameter. During normal operation, the APA is given a slight negative voltage of -20 V so all the contact pairs are pressed against each other. The FMS is opened by applying a voltage of $+150$ V to the APA, which elongates the stack and causes the elliptical shell to contract and separate the contacts. The contacts of the FMS achieve their full separation of 500 μm at around 500 μs .

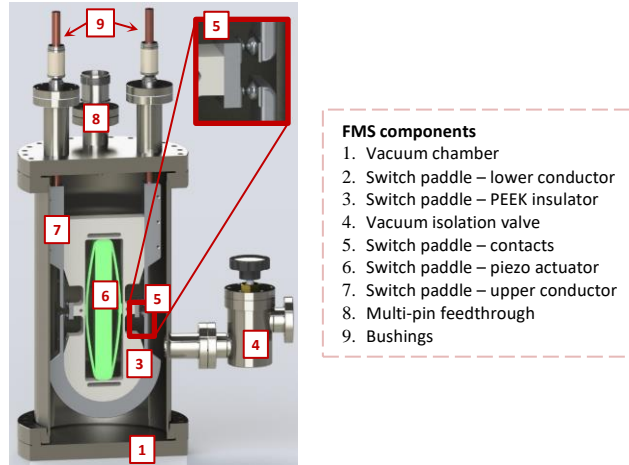


Figure 3 - Section view of the FMS prototype with all the components– patents pending [51-53].

Figure 4 shows a proposed FMS based on linear piezoelectric actuator. The actuator is enclosed in a pressure chamber containing supercritical carbon dioxide (CO₂), which is shown to have high dielectric strength, low viscosity, and outstanding thermal properties. The temperature and pressure in the chamber are 32°C and 7.5 MPa respectively [54]. During normal operation, the actuator is given a positive voltage to press the moving contacts against the fixed contacts attached to the high-pressure bushings. The FMS is opened by removing the applied voltage, which contracts the actuator stack and opens the contacts to its full separation of 100 μm in less than 250 μs.

Table 1 - Comparison OF Piezoelectric FMS TYPES

Characteristics	APA FMS	Linear Piezoelectric FMS
Stroke	500 μm	100 μm
Dielectric Medium	Vacuum	Supercritical CO ₂
Opening Time	500 μs	250 μs
Operating Pressure	<10 ⁵ mbar	30 bar
Contact Force per pair	27 N	>250 N
Contact Diameter	5 mm	10 mm

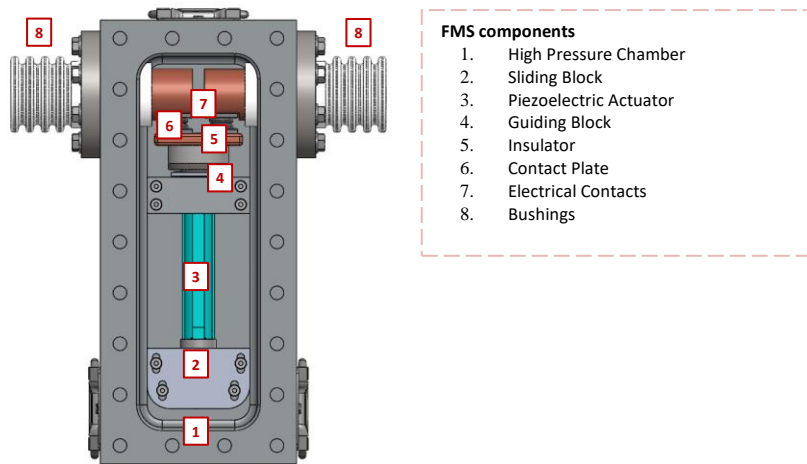


Figure 4 - Section view of the FMS prototype based on linear piezoelectric actuator [55].

The APA FMS operates in vacuum at a pressure less than 10^{-5} mbar. The linear piezoelectric FMS operates at a pressure of 7.5 MPa and temperature above 32°C. APAs have a higher stroke than a linear piezoelectric stack, which results in a higher voltage rating of the FMS when operated in the same dielectric medium. However, this comes at the cost of reduced force between the contact pairs, which increases the contact resistance and limits the current rating of the FMS. The reduced opening force of APAs also limit the size of the contacts, which further restricts the achievable current rating. This research effort explores the design considerations associated with piezoelectric FMS based on the dimensions, blocked force and stiffness of the APA, and linear piezoelectric actuators. The design tradeoffs of the piezoelectric actuator sets the constraints on the design of electrical contacts for the FMS.

2.4 Electrical Contacts

The FMS is expected to carry up to a few kiloamperes of nominal current, withstand a rapidly rising fault current before commutation, and withstand the transient recovery voltage by achieving full contact separation of at least an order of magnitude faster than conventional circuit breakers. As a result, electrical contacts are a key component that have significant impact on the performance of the FMS. The existing prototypes of FMS borrow from research on contacts of conventional AC circuit breakers such as SF₆ and vacuum circuit breakers. However, the stress characteristics experienced by FMS contacts are different from the stress characteristics that contacts experience in conventional breakers. One key difference is that FMS is a non-arcing device as opposed to conventional circuit breakers, which are design to handle the switching arcs. This has implications for contact design considerations relating to a geometry, resistance, material erosion and durability when exposed to repeated electric arcs are no longer applicable. The low separation between the contacts emphasizes the need to avoid electric field enhancement in the gap. The smaller size of contacts (to enable high opening speed) and FMS being used primarily in DC and high fault current applications means that the thermal stress on contacts could be greater compared to similarly rated conventional AC breakers. The increased thermal stress can cause wear damage due to heating and cooling driven microslips [56] and sticking/welding of contacts due to exposure to rising fault current [57] before commutation. The material and geometry of the contacts must be selected by taking these factors into consideration.

SF₆ circuit breakers typically use contacts made of silver based refractory materials such as AgW, AgWC and CuW [58] and vacuum breakers typically use CuCr [59] contacts. Prior literature on best contact materials focus on analytical and experimental methods [60] for material selection with high importance given to the ability of contact materials to withstand wear damage and erosion caused by electric arcs [61]. The contacts materials used in conventional circuit breaker may not necessarily be the optimal material choice for the non-arcing FMS contacts. This dissertation identifies the most suitable contact materials by a materials selection process known as the “Ashby method” [62]. The materials are ranked based on the relative importance of the FMS requirements.

The geometry of the contacts must result in nearly uniform electric field to minimize the risk of electric breakdown when the contacts are open. Geometries such as those proposed by Bruce, Rogowski [63-66], Ernst and Chang [67-69], which were developed to make electrodes for applications that require uniform electric fields in physics experiments, can be used. These geometries will also have a greater real area of contact for a given force between the contacts and similar surface roughness. This reduces the constriction of current flowing through the contacts and results in a lower contact resistance than spherical contacts [70]. This dissertation presents contact geometries that minimize electric field enhancement and contact resistance.

Furthermore, the electrical contacts of piezoelectric FMS are susceptible to fretting wear due to low contact forces. Fretting wear is defined as the relative cyclic displacement between two surfaces, having a non-uniform distribution of local relative displacement at their contact. Fretting wear and fretting fatigue can arise due to vibration, cyclic loading or

cyclic temperature changes. Fretting wear is typically not studied for AC circuit breakers because the wear in AC breakers is dominated by the damage to the contacts from arcing and arc erosion. In non-arcing FMS, fretting becomes the dominant wear mechanism. Prior literature has demonstrated that fretting increases the resistance between two surfaces over time. Fretting is found to increase the resistance between surfaces of contacts and connectors over time under AC and DC currents [71]. For copper contacts, the results show the increase in contact resistance shows no difference under AC and DC current. Therefore, it is unlikely that magnetic forces by electric field on AC currents will have an impact on fretting wear. The surface properties of the fretting scar can reduce the breakdown voltage of the FMS due to localized electric field enhancement. The impact on the contact surface after fretting wear under DC current on the contact resistance and breakdown voltage between the contacts is studied.

The performance of the contacts can also be improved by using a contact pair made of dissimilar materials. Similar materials, due to their chemical affinity towards each other, tend to have strong adhesive bonds. When two dissimilar materials are used, the inherently lower chemical affinity results in weaker adhesive bonds, which reduces the wear [72]. This idea has been proposed for motor relay contacts with AgCd/AgCdO contacts [73]. The reduced fretting wear can result in lower contact resistance between dissimilar contact pairs. The extent of reduction in contact resistance is studied experimentally.

Another advantage of using dissimilar materials in a contact pair is the ability to control the direction of flow of heat, which is known as thermal rectification [74]. Thermal rectification can reduce the temperature of the contacts by directing the heat flow outside

the FMS chamber. The degree of thermal rectification and wear damage in dissimilar materials are known to be affected by surface roughness, coefficient of thermal expansion, thermal conductivity, contact geometry, and lattice structure of both materials in a dissimilar pair [75]. The extent of thermal rectification from dissimilar contact pairs and the subsequent improvement in performance of FMS is studied thorough experiments and simulation models.

Careful selection of the material and geometry of the contacts can have a significant impact on the performance of FMS. This dissertation describes the results of research on contact materials and geometry to improve the performance of FMS.

CHAPTER 3. RESEARCH OBJECTIVES

The objectives of the proposed research are:

- Determine the design considerations specific to piezoelectric FMS and the constraints they impose on contact design (Chapter 4)
- Identify the most suitable electrical contact materials for piezoelectric FMS based on a systematic approach (Chapter 5)
- Identify the most suitable geometry for electrical contacts that minimizes electric field enhancement and contact resistance (Chapter 6)
- Understand the impact of fretting wear on the breakdown voltage of the electrical contacts when they are open (Chapter 7)
- Understand the impact of using dissimilar contact materials in a contact pair on contact resistance after fretting and thermal rectification (Chapter 8)

The outline of the succeeding chapters is below:

- Chapter 4 investigates the considerations for designing piezoelectric FMS through physics-based simulations and the constraints they impose on the design on electrical contacts.
- Chapter 5 presents a systematic approach to identify the most suitable contact materials for piezoelectric FMS based on the requirements of the FMS and ranks the materials based on importance of each requirement.

- Chapter 6 presents optimized contact geometries that can minimize the electric field in the contact gap when the contacts are open through finite element simulations and minimize contact resistance when the contacts are closed through experiments.
- Chapter 7 presents the effect of fretting wear on the breakdown voltage of piezoelectric FMS contacts through finite elements simulations of randomly generated contact surfaces based on the surface properties of contacts after fretting experiments.
- Chapter 8 presents the impact of using dissimilar contact materials in a contact pair on the contact resistance when exposed to fretting wear and on controlling the direction of flow of heat in the FMS.
- Chapter 9 draws broad conclusions of this dissertation
- Chapter 10 discusses the future outlook of this research and the potential topics that need to be studied for further understanding of designing contacts for FMS.
- Chapter 11 lists all the publications and patents by the author.

CHAPTER 4. DESIGN CONSIDERATIONS FOR PIEZOELECTRIC FMS

4.1 Motivation

In this chapter, the design considerations for APA FMS are explored using physics-based simulations. The results are used to guide the design of electrical contacts for FMS. Figure 5 shows the key design considerations of piezoelectrically actuated FMS in a 3-D graph. The three key design parameters of the piezoelectric actuator are its stroke, blocked force and the response time, which affects the voltage rating, current rating and di/dt withstand rating of the FMS respectively. A higher stroke results in a larger separation between the contacts of the FMS, which leads to higher voltage rating. A faster response time results in the FMS opening before the fault current reaches a high value. So the FMS is able to interrupt faults with higher di/dt . A higher blocked force results in higher contact forces between the contact pairs of the FMS as more force is available to move the contacts. A higher contact force leads to lower contact resistance and hence higher current rating of the FMS. The stroke, stiffness/blocked force, and response time depend on the dimensions of the APA. The dimensions of the APA affects the power density of the FMS. This chapter shows the design tradeoffs of APA FMS using physics-based simulations. These tradeoffs affect the design of electrical contacts for FMS.

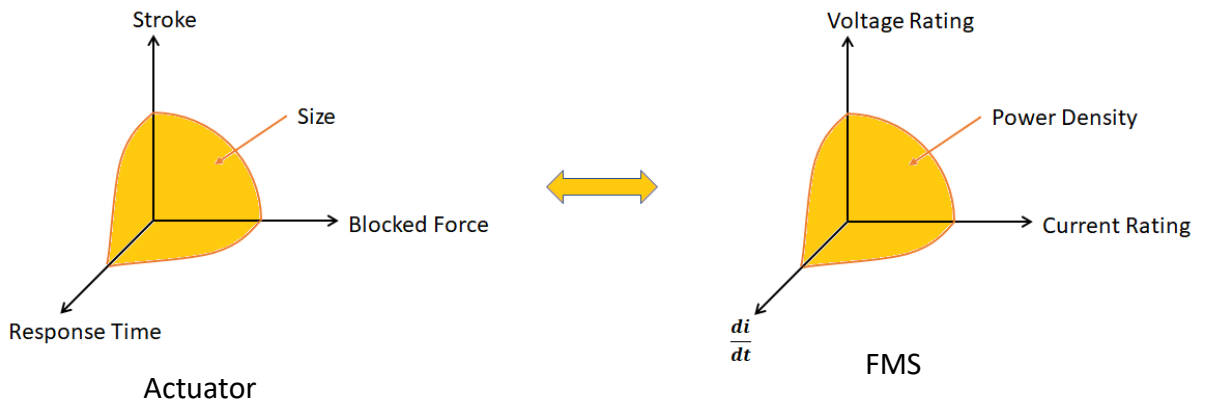


Figure 5 - Design considerations for piezoelectric FMS

4.2 Piezoelectric FMS Concept and Operation

Figure 6 shows a commercial APA, which consists of a stainless-steel elliptical shell around the linear piezoelectric actuator. The actuator consists of stacks of piezoelectric material which are mechanically in series. The electrical analogue of the series connected piezoelectric stacks are parallel connected capacitors. The application of voltage across the piezoelectric stack results in expansion across the major axis, which leads to contraction in the minor axis. Piezoelectric actuators can move with accelerations of over 10,000 m/s², but the velocity is limited by the speed of sound in the crystal (1-6 km/s). As a result of the inertia of possible coupled masses and of the actuators themselves, dynamic tensile forces occur during actuations, which are compensated by compressing forces, generally created by preloading the actuator. The maximum force generated by the actuator is known as the blocked force. It is achieved when the stroke of the actuator is completely blocked, i.e. against a load with an infinitely high stiffness. The actual force generated in practical conditions is lower than the blocked force. For APA, the actuator design hinges around the

size (length and cross section) of the piezoelectric stack, and the aspect ratio of the elliptical shell. The greater the aspect ratio, the higher the amplification and therefore the prospective stroke. However, greater aspect ratio also reduces the blocked force and increases the response time. The reduced blocked force will also result in lower contact forces, which increases contact resistance and hence power loss in the FMS. Increasing the size of the stack increases the mass of size of FMS, the capacitance of the actuator and therefore the required driving current and the cost of the actuator.



Figure 6 - Amplified Piezoelectric Actuator [76]

The FMS consists of fixed contacts, attached to the terminals of the switch, and moving contacts, attached to the minor axis of the APA. The current in the FMS flows from one terminal to another through the four contact pairs. In the default state, the contacts touch each other at zero force. The moving contacts are separated by the contraction of the minor axis of the APA. The contacts are pressed against each other in the closed state through the contraction of the actuator stack to reduce the contact resistance. The contact force depends on the blocked force available for expansion of the actuator in the open state. A higher blocked force results in a high opening speed of the FMS. The maximum stroke between a single pair of contacts achieved by an APA FMS prototype in literature is 0.5

mm. This requires the FMS to operate in a medium of high dielectric strength for medium and high voltage applications. The total contact separation in the FMS can be increased by having multiple contact pairs that are electrically in series. The stroke is also affected by the mass of the moving contact system.

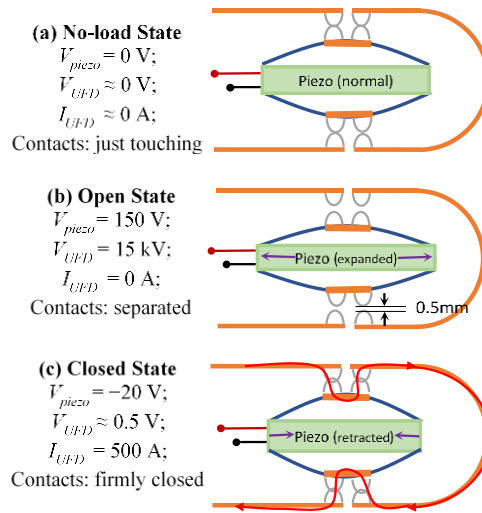


Figure 7 - Opening and closing mechanism of an amplified piezoelectric actuator in FMS

4.3 Static Simulation Models

The piezoelectric actuator used in simulations is based on the dimensions of a Cedrat APA used in the FMS prototype in [46, 47]. Simulation models of the piezoelectric stack itself depends on material properties that are not publicly communicated by the manufacturer. As a result, only the elliptical shell around the stack – which is made of an unspecified type and temper of stainless steel – is simulated using solid mechanics and spring-mass-damper simulations with the dimensions and blocked force of the piezoelectric actuator obtained from the datasheets.

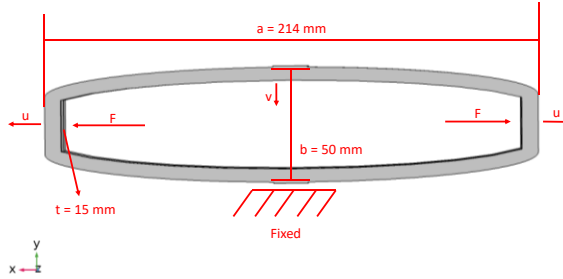


Figure 8 - Actuator Shell Simulation Model

The diameters of the major and minor axis are denoted by a and b respectively and the thickness of the actuator shell is denoted by t . The actuator in the FMS prototype has $a = 214$ mm, $b = 50$ mm and $t = 15$ mm. For the simulations, the value of a is fixed at 214 mm. The force is applied on either end of the major axis, causing a deformation of the minor axis as shown in Figure 8. A fixed constraint is applied to one end of the minor axis to determine the stroke at the other end. Dimensions b and t are varied along with the blocked force F to determine the stroke in the minor axis, denoted by v . As it is a static model, the absolute location of the fixed constraint does not matter as long as there is only one fixed constraint. The model measures the final stroke of the actuator shell. The stroke as a function of the blocked force is used to calculate the stiffness of the actuator shell. Similar studies on APA's have been performed in [77, 78], where the APA is used for different applications such as microgrippers and servo valves.

The proposed simulation model has the following limitations: By not modelling the piezoelectric stack, there is no boundary condition for the velocity of the actuator, which is limited by the speed of sound. The stiffness of the actuator stack is also limited by the compressive strength of the actuator. The Young's modulus of the actuator stack depends

on its cross section. However, by conducting a parametric sweep of b , t and F with values close to that of a real actuator, the limits with respect to velocity, stiffness and cross section of the actuator stack are not exceeded.

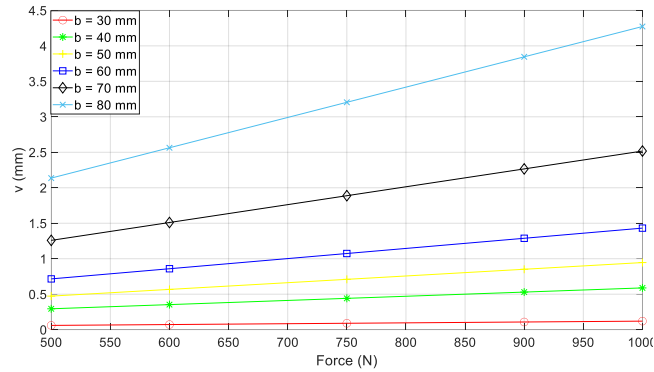


Figure 9 - Actuator Shell Stroke vs. Force at a thickness of $t = 15$ mm

Figure 9 shows the stroke v as a function of the force and the diameter of the minor axis. This thickness t is set to 15 mm. The stroke increases linearly with force and reduces when the diameter of the minor axis is increased. The stiffness of the actuator shell, which is the inverse of the slope of Figure 9, decreases as the diameter of the minor axis increases.

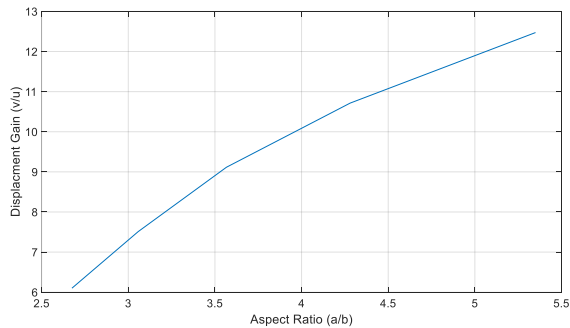


Figure 10 - Actuator Shell Stroke Gain vs Aspect Ratio

Figure 10 shows the stroke gain (v/u) as a function of the force and the aspect ratio of the actuator (a/b). The stroke gain is unaffected by the force and is only affected by the aspect ratio of the actuator shell. The stroke gain increases with higher aspect ratio of the shell so actuators with higher b have lower stroke gain. However, there are some practical considerations to the maximum b achievable due to the plateauing of the stroke gain at high aspect ratios.

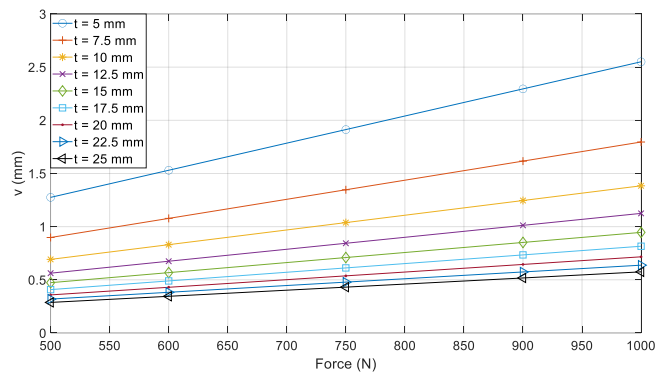


Figure 11- Actuator Shell Stroke vs. Force at a fixed minor axis dimension of $b = 50$ mm

Figure 11 shows the stroke v as a function force for different thickness of the actuator. The diameter of the minor axis b is set to 50 mm, the same as the APA1000XL actuator. The stroke is greater when the thickness of the actuator shell is lower, as this decreases the mass of the actuator. Figure 12 shows the stroke v as a function of thickness t of the actuator for different aspect ratio at $F = 750$ N. The stroke is greatest when the aspect ratio is the lowest at low thickness. The stroke falls rapidly for high values of b as the thickness is increased and is almost constant with respect to thickness at low values of b .

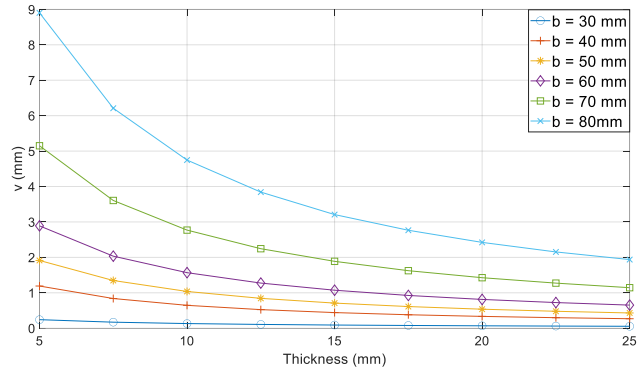


Figure 12 - Actuator Shell Stroke vs. Thickness at 750 N force.

The results from the static simulations show that for any given length of the major axis of the actuator shell, the stroke of the actuator can be increased by increasing the force and the aspect ratio. The stroke is also increased by reducing the thickness of the actuator. However, the aspect ratio changes the response time of the actuator, which is not captured in the static simulations. Also, the response time is affected by the natural damping by the actuator and the mass of the contacts connected to the actuator. These results are studied using a spring-mass-damper system simulation in MATLAB/Simulink's Simscape (version? REF?) environment.

4.4 Dynamic Simulations

According to the displacement versus force results in Figure 9 and Figure 11, the stiffness of the actuator shell is calculated. Figure 13 shows the stiffness of the actuator shell as a function of thickness and width of the shell. The stiffness is higher at lower width and increases with thickness.

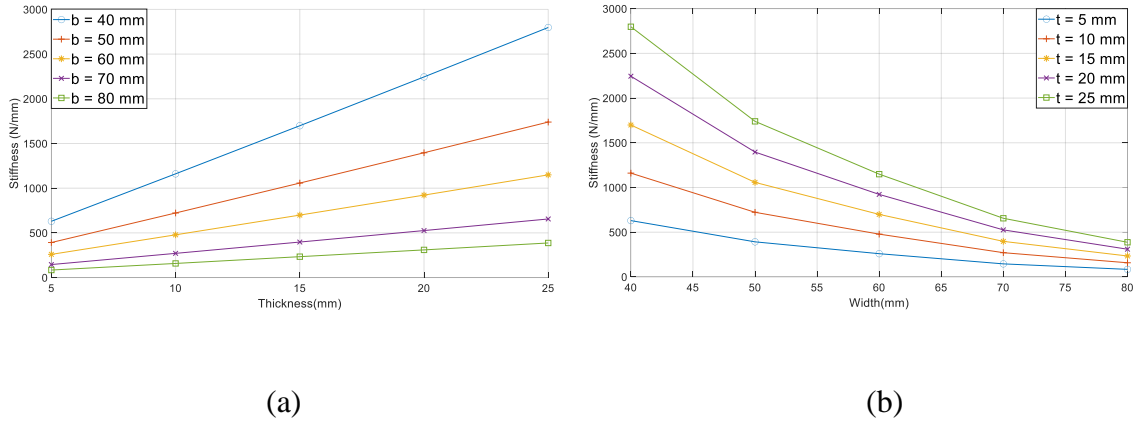


Figure 13 - Stiffness of the actuator shell at different thickness and width

The critical damping ratio of the actuator shell can be calculated using the formula:

$$C_c = 2\sqrt{km} \quad (6)$$

where m is the mass of the actuator, k is the stiffness of the actuator. C_c is calculated for all values of b and t . Subsequently, the actuator shell is simulated as a spring-mass-damper system in Simscape as shown in Figure 14. The spring-mass-damper simulations are used to obtain the travel curve of the actuator.

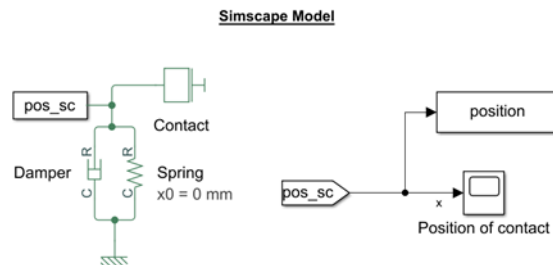


Figure 14 - Simscape model of the simplified spring mass system

The mass pulled by the spring damper simulation shown in Figure 14 is the mass of the moving contacts. Based on piezoelectric FMS prototypes in prior literature, the mass is varied from 0.05 – 0.3 kg to study the travel curve. The values of spring constant k and damping coefficient C_c are based on the width and thickness of the actuator shell. The travel curve for the contacts is obtained as a function of contact mass and actuator dimensions.

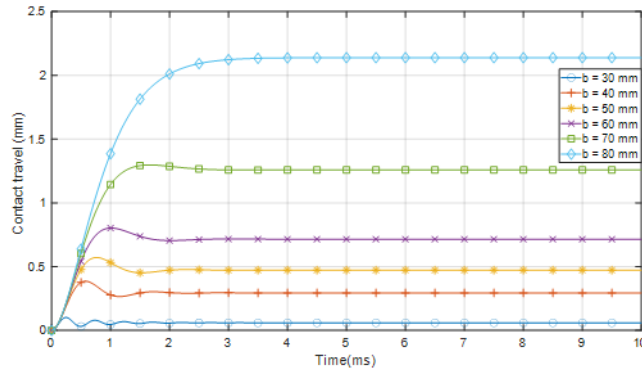


Figure 15 - Contact travel curves with different width of actuator shell

Figure 15 shows the travel curve of contacts with a mass of 0.05 kg at $t = 15$ mm and a force of 500 N. The travel curves have identical velocity until the contacts cross their steady state stroke. The actuator shell with higher widths take longer to reach their highest contact separation. However, they also reach their steady state contact separation with minimal contact bouncing. Figure 16 shows the travel curve of contacts with a mass of 0.05 kg at $b = 50$ mm and a force of 500 N. The contacts have a high overshoot and bounce at lower thickness of the actuator shell. Actuators with lower thickness may still be preferred as the overall contact separation is always higher. However, depending on the type of commutation process used by the overall HCB, a linear travel curve with minimal

contact bounce may be preferred if, for instance, the semiconductors in the HCB are tripped sequentially [79].

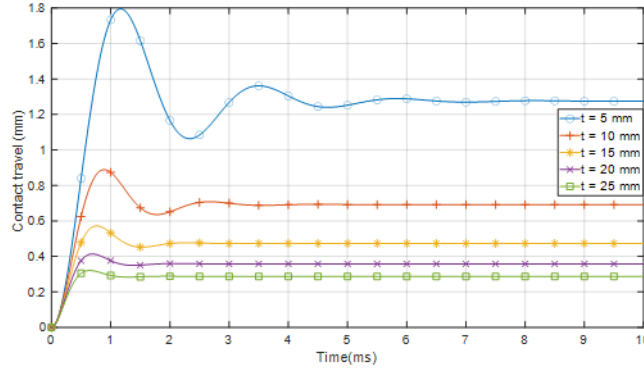


Figure 16 - Contact travel curves with different thickness of actuator shell

Figure 17 shows the travel curve of contacts of different mass at $b = 50$ mm, $t = 15$ mm and force of 500 N. The lower mass of contacts results in contacts taking less time to fully separate. Contacts with higher mass reach a larger contact separation due to its inertia but this overshoot comes at the cost of contact bounce. The mass of the contacts is varied between 0.05 – 0.3 kg, which is in range of the 0.15 kg contacts used in FMS prototype in Figure 3. As a result, the response time is in the underdamped region. Increasing the mass further would result in an overdamped response with no contact bounce, but such a high mass would reduce the time taken to reach full stroke or fail to open with the limited blocked force of the actuator. Contact bounce can reduce the separation distance and makes the FMS more susceptible to electric breakdown due to transient recovery voltage. As the contact shape is optimized to reduce electric field enhancement at its corners [80], the mass of contacts is directly proportional to the area of contact between a contact pair. Contact geometries with larger areas of contact have lower contact resistance [70]. This results in

a trade-off that needs to be achieved in contact design, where larger mass results in better current rating but lower voltage rating.

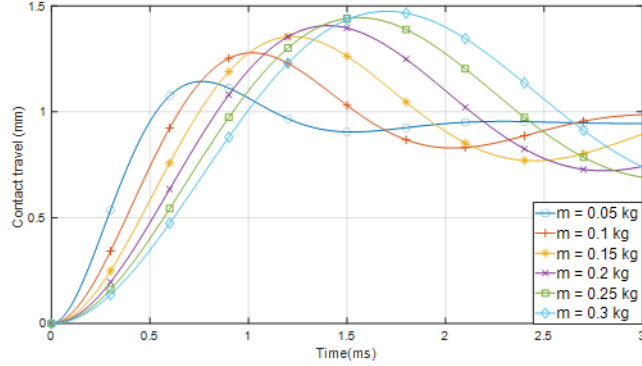


Figure 17 - Contact travel curves with different mass

4.5 Summary

The main design parameters of the APA are the stroke, blocked force, and the response time. These parameters directly affect the voltage, current and di/dt rating of the piezoelectrically actuated FMS. The actuator parameters depend on the size and dimensions of the actuator, which in turn affects the power density of the piezoelectrically actuated FMS. This chapter demonstrated the method to trade-off different actuator characteristics to build the FMS. The results show that actuators with lower thickness and higher diameter of minor axis have larger stroke. However, they also have higher contact bounce and the contacts take longer to reach their steady state separation distance. The mass of the contacts was also found to affect the travel curve with lighter contacts separating faster and with lower bounce. The overshoot in the travel curve increases with contact mass which makes the FMS susceptible to restrike by transient recovery voltage.

Furthermore, for the same contact material, lighter contacts also have lower area of contact and hence lower current ratings.

The physics of the piezoelectric actuator stack is not modelled in this paper and including it in the model can lead to more accurate results. The study can be expanded for other types of piezoelectric actuators such as linear piezoelectric stacks, APAs with a rhombus shell [81] and nested actuators[82]. The determination of limits on contact mass due to a tradeoff between the current and voltage rating of the FMS can be explored in more detail by considering different contact materials. Contact materials with low density, low resistivity and high elastic modulus are preferred to maximize voltage and current ratings. However, no single contact material may have all the desired properties and a trade-off may be necessary in the selection of the contact material [83].

CHAPTER 5. ELECTRICAL CONTACT MATERIAL SELECTION

5.1 Motivation

A key challenge in the design of the FMS is to identify electrical contact materials that can withstand the electrical, thermal, and mechanical stresses on the FMS. The FMS must have electrical contacts with a large contact surface area to operate at the rated DC current without overheating. However, the contact mass also affects the acceleration and travel time for a given actuator characteristics, which limits the useful upper range of the contact surface area. Furthermore, the use of piezoelectric actuators results in lower contact forces between contact pairs. The lower contact forces make the FMS more susceptible to fretting wear [11] than conventional disconnect switches, especially in applications in the transportation sector, in which mechanical vibrations are more prevalent than in stationary applications. The smaller size of the contacts also make them susceptible to overheating and melting due to increased thermal stress. Therefore, the contacts should be made of materials that combine high electrical and thermal conductivity with the ability to withstand wear and melting during normal and short circuit conditions. The material selection problem has different constraints compared to that of conventional AC breakers, which are designed to withstand arcing but have switching speeds that are typically at least an order of magnitude lower than FMS.

In this chapter, a systematic material selection approach known as the Ashby method is used to identify and rank the most suitable contact materials for FMS. The desired performance features of the FMS – such as lower power loss, fretting wear and melting – are translated into objectives, constraints, and free variables, which are used to derive materials indices. A large database of materials is screened using the material indices to rank the most suitable contact materials for FMS. As the requirements for FMS contact materials are different from conventional circuit breakers, the work presented in this paper serves as the basis for future research in this area. As the FMS is a new type of switch in early stages of research, a systematic study to identify the best contact materials has yet to be conducted. This chapter identifies the best materials that will minimize power loss, wear and overheating. The top ranked materials are to be further investigated in the future through test data, analyses, availability, pricing, etc. to help to reduce the number of candidate materials to a level that is manageable for experimental validation.

5.2 Ashby Method

The goal of material selection processes is to perform an optimization to identify the most suitable material for an application based on competing requirements and constraints. Several material selection methods have been proposed in literature, all of which are based on Multiple Criteria Decision Making (MCDM) [84]. These methods can be broadly categorized into analytical methods and quantitative methods. Analytical methods, which are considered as Multiple Objective Decision Making methods (MODM), uses a combination of equations and graphical techniques to identify the most suitable materials. The most popular analytical method is the Ashby method. Quantitative methods, which are

considered as Multiple Attribute Decision Making methods (MADM) use computer aided techniques to perform for selection of suitable materials [85]. The most popular quantitative methods are *ViseKriterijumska Optimizacija I Kompromisno Resenje* (VIKOR) [86] and Technique for Order of Preference by Similarity to Ideal Solution (TOPSIS) [87]. Analytical methods are more suitable as a ‘first screen’, where suitable material solutions are selected from a large database consisting of all material types like metals, ceramics, glasses, polymers, elastomers, and hybrids. The material selection process screens and ranks a large database of materials based on the material indices derived for the most important objectives. The quantitative methods are more suitable as a ‘second screen’ to select the best composition of the materials from the suitable material candidates. The material selection process identifies the best solution among the available choices. The quantitative methods require more information about the materials such as all the available compositions of a particular material, details about the microstructure and its effect on material properties. Such information on the most common electrical contact materials are not easily available. As a result, the Ashby method is used to identify suitable material solutions for electrical contacts of FMS. The disadvantage of the Ashby method is that it requires a significant amount of work to derive all the material indices. Hence, only the most important materials indices are derived in this analysis.

According to the Ashby method, the performance of a material for any engineering application is given by its performance index

$$P = f(F, G, M) \quad (7)$$

where f is the function of Functional (F), Geometric (G) and Material (M) parameters. These parameters are independent of each other and the overall performance of the materials depends on the collective output of individual parameters. The performance of the material can be maximized for all F and G by optimizing the material parameters or material index. The four steps of the Ashby method are:

1. Translate the design requirements as objectives, function, constraints, and free variables.
2. Screen the materials using constraints by eliminating materials that do not satisfy design requirements.
3. Rank the materials using objectives.
4. Seek supporting information by a detailed study of the top ranked materials.

The material selection is performed on a large database of materials by Granta Design. The database consists of 3985 materials consisting of metals, ceramics, glasses, polymers, elastomers, and hybrids. The CES Edupack software [88] by Granta Design is used screen and compare the materials based on the derived material indices. Only the first three steps of the Ashby method are used to identify the best materials for FMS, as this is a more general selection process. The fourth step, seeking documentation, involves further investigation of the top ranked candidates through familiarity of typical applications, failure modes, test data, analyses, availability, pricing, among others to help thin out the list to one or two solutions. The material selection problem is a multi-objective

optimization problem and Pareto optimization technique is used to identify suitable materials [89]. The Pareto optimal solution is a set of all non-dominated solutions from a given solution space. The non-dominated solutions are identified using tradeoff plots. In the tradeoff plots, the inverse of the material indices for each objective is plotted for better visualization. That is, the lower the value of the objective, the more viable the material. A Pareto optimal solution based on assigning weights to different objectives will be required to identify the most suitable material.

Prior research has focused on selection of contact materials RF MEMS switches, AC circuit breakers, and electrical connectors. Suitable materials have been identified based on the Ashby method, as well as other analytical and experimental methods. Table 2 summarizes the different applications and material selection methods used to identify suitable contact materials. The analytical methods include finite element analysis and other mathematical approaches to estimate the range of required material properties. The contact materials whose material properties are in this range are selected. The experimental methods conduct standardized tests on several (<10) materials and select the best materials based on the results. The analytical and experimental methods cannot be scaled to select the best material candidate among thousands of materials. They require a pre-screening step to reduce the number of candidate materials to a reasonable number. To select the best material for a new application, it is necessary to cast a wide net to not overlook new or unlikely material candidates. Methods such as the Ashby, VIKOR and TOPSIS [90] are used to screen and select the promising materials solution when there are multiple and conflicting objectives from a large database of materials. As the criteria for selecting

electrical contact material for FMS are multiple and conflicting, the Ashby method is used in this paper.

Table 2 – Electrical contact material selection approaches for different application

Author	Electrical Contact Application	Material Selection Method
Buggy et al. [91]	Electrical Connectors	Analytical
Heitzinger et al. [59]	Vacuum Interrupters	Analytical + Experimental
Frey et al. [92]	Vacuum Interrupters	Experimental
Watkins et al. [93]	High Power Switches in EM Launchers	Ashby method
Amft et al. [94]	Low voltage contactors	Analytical
Coutu et al. [95]	MEMS Switches	Analytical
Sawant et al. [96]	RF MEMS Switches	Ashby method + Experiment
Deshmukh et al. [97]	RF MEMS Switches	Ashby, TOPSIS and VIKOR method

5.3 Material Selection Process

5.3.1 Translation Table

FMS generally have a pair of contacts, which are identical in geometry and material. While the contacts of FMS can have different geometries to minimize electric field and contact resistance [65, 98], this analysis is meant to be independent of the geometry of the contact material. The most important features of the electrical contact materials are:

1. Low power loss
2. High wear resistance
3. High resistance to overheating during short circuit

The contact material should also have a high work function to minimize electric breakdown in the gap by electron field emission. However, the work function of all commonly used contact materials (conductive metals and alloys) are in a similar range (4-6 eV), so it is not considered in the material selection process. Also, the dominant damage mechanisms on the contacts are mechanical rather than electrical, as the FMS opens at zero current with no arcing. With this information, the material selection problem can be set up as a multiple objective problem. The translation table is shown in Table 3.

Table 3 – Translation Table

Function	Light-Conductive-Wear Resistant Contact Material
Objective	<ul style="list-style-type: none"> • Minimize resistive loss • Minimize wear • Minimize contact overheating
Constraints	<ul style="list-style-type: none"> • Good electric conductor (<10 $\mu\Omega\cdot\text{cm}$) • Good thermal conductor (173 W/mK) • High hardness (>100 HV) • The force between the contacts is specified. • The current carried by the contacts is specified. • The dimensions (length/radius, area of contact) of the electrical contacts are specified.
Free Variables	Choice of Material

5.3.2 Derivation of Material Indices

The first objective is to minimize the power loss P in the contacts, which is expressed as $P = I_0^2 R$, where I_0 nominal current through the FMS and R is the resistance of the contact pair. The contact resistance R is a function of the resistivity, geometry, surface roughness and contact force. The force between contacts is specified for a given type of

FMS. Also, it is assumed that the materials considered can all be machined to any desired surface roughness so the effect of the real area of contact between a contact pair can be neglected. While there is no general equation to calculate the prospective contact resistance of an arbitrary geometry, it is clear that the resistance is directly proportional to the resistivity of the material.

$$R = C \cdot \rho_c \quad (8)$$

where ρ_c is the resistivity of the material, and C is the constant of proportionality that depends on the geometry. Substituting the equation for resistance in the objective equation, we get

$$P = CI_0^2 \rho_c \quad (9)$$

Since the current through the contacts is specified and the analysis is independent of the geometry of the contact, the material index is

$$M_1 = \rho_c \quad (10)$$

which is to be minimized.

The second objective is to minimize wear experienced by contacts. The contacts experience electrical, mechanical and thermal stresses which lead to different types of wear. The wear types experienced by the contacts according to the classification in [99] are:

1. Fretting wear due to micro-slips at the contact interface
2. Impact wear due to closing of contacts at high speed

The fretting wear is caused by micro-slips at the interface of the contacts due to mechanical vibrations, thermal expansion and electrodynamic forces. Studies have shown that fretting wear depends on the fretting frequency, current load, normal force, slip amplitude and temperature of the contacts [100]. The contact resistance has been shown to increase by at least an order of magnitude after the onset of fretting damage. The number of cycles to failure by fretting has been shown to be lower under higher thermal stress [101], which is expected in all FMS, and lower contact force [102], which is expected in piezoelectric FMS. This is the most dominant wear mechanism capable of causing most damage. The FMS is also subject to impact wear when the contacts close at high speed. The FMS, like most circuit breakers and vacuum interrupters, is expected to be rated for 20,000 operations and have a lifetime of 20 years. This means about 1000 operations per year on average. The low number of expected switching operations make impact wear the less dominant wear mechanism.

Fretting wear follows the Archard's wear equation, which is given by

$$Q = K \frac{NL}{H} \quad (11)$$

where Q is the volume of wear debris, K is the dimensionless wear coefficient, L is the sliding distance, N is the force between the contacts and H is the hardness the material. In the case of fretting, the sliding distance L is proportional to the amplitude of micro-slip at the interface of the contacts, which is, in turn, proportional to the contact stiffness (can be represented as Young's modulus, E), and is inversely proportional to load N [103].

The dimensionless wear coefficient K is defined as the probability of each asperity interaction resulting in the production of a wear particle. K depends on the material properties, geometry of the contact zone, surface roughness and testing conditions and the exact value of K is not available for many candidate contact materials under uniform conditions. Considering the unavailability of K for all the candidate materials, the second material index is assumed to be

$$M_2 = \frac{E}{H} \quad (12)$$

which is to be minimized.

The impact wear of contact surfaces, while not being the dominant wear mechanism, is also thought to decrease with decreasing M_2 . Increasing hardness leads to increase in material strength, and, hence, to decrease of surface damage. Decreasing Young's modulus leads to increase in material compliance, and, hence, to an accommodation of impact energy through elastic deformation rather than through

interfacial slip and generation of structural defects. Thus, the material index M_2 covers both fretting and impact wear.

The third objective is to minimize overheating of contacts during short circuit, which can cause the contacts to melt and/or weld together. The contacts are susceptible to overheating when there is rapid rise in current due to a fault. Based on the current interruption process of HCB in Figure 1, the contacts of the FMS are exposed to fault current until the current commutation switch opens and moves the current to the semiconductor branch. Therefore, the heat energy produced by the fault is assumed to be

$$E_{in} = \int_0^t I_f^2(t)R(t)dt \quad (13)$$

where E_{in} is the heat energy produced by the fault, I_f is the instantaneous fault current across the FMS, R is the contact resistance and t is the time between the inception of the fault and commutation. The energy produced can be assumed to be not greater than

$$E_{in} \cong I_p^2 R t \quad (14)$$

where I_p is the peak fault current rating of the FMS, which is specified. The material index is derived through the energy balance equation given by

$$E_{in} = E_{out} + E_{absorbed} \quad (15)$$

where E_{out} is the heat energy removed by conduction and $E_{absorbed}$ is the heat energy absorbed by the contacts, which causes overheating. Due to rapid rise of heat and short time duration of faults, it is assumed that there is insufficient time to conduct heat away from the contacts. The thermal energy stored in the contacts is given by

$$E_{absorbed} = \rho V C_p \Delta T \quad (16)$$

where ρ is the density of the contact material, V is the volume, C_p is the heat capacity and ΔT is the rise in temperature. The equations for E_{in} and $E_{absorbed}$ are equated which results in

$$\Delta T = \frac{I_p^2 R t}{\rho V C_p} \quad (17)$$

The impact of the rise in temperature is material dependent. A material with a high melting point exposed to the same temperature will not cause the same amount of surface damage as a material with a lower melting point. So ΔT is normalized by the melting temperature T_{melt} to give homologous temperature rise

$$\frac{\Delta T}{T_{melt}} = \frac{I_p^2 R t}{\rho V C_p T_{melt}} = \frac{I_p^2 C \rho_c t}{\rho V C_p T_{melt}} \quad (18)$$

The third material index is therefore given by

$$M_3 = \frac{\rho_c}{\rho C_p T_{melt}} \quad (19)$$

which is to be minimized. Considering that M_1 is part of M_3 , we can proceed to further analysis based on material indices M_2 and M_3 only.

This limits the subset of materials to 95, which is a much more manageable number. Figure 18 shows the tradeoff plot for M_2 vs M_3 . Materials close to the tradeoff curve and other well-known materials are labelled. The white ovals represent materials in the CES database and the black ovals represent materials added to the database (AgW, AgWC, CuW). The ideal material solution should be found on the bottom left corner of the charts. If no material solution exists in this region then the materials near the tradeoff surface offer the best compromises. The large gap in the bottom left area indicates that there is no ideal material solution. However, it is possible to rank the contact materials based on the relative importance of the performance indices.

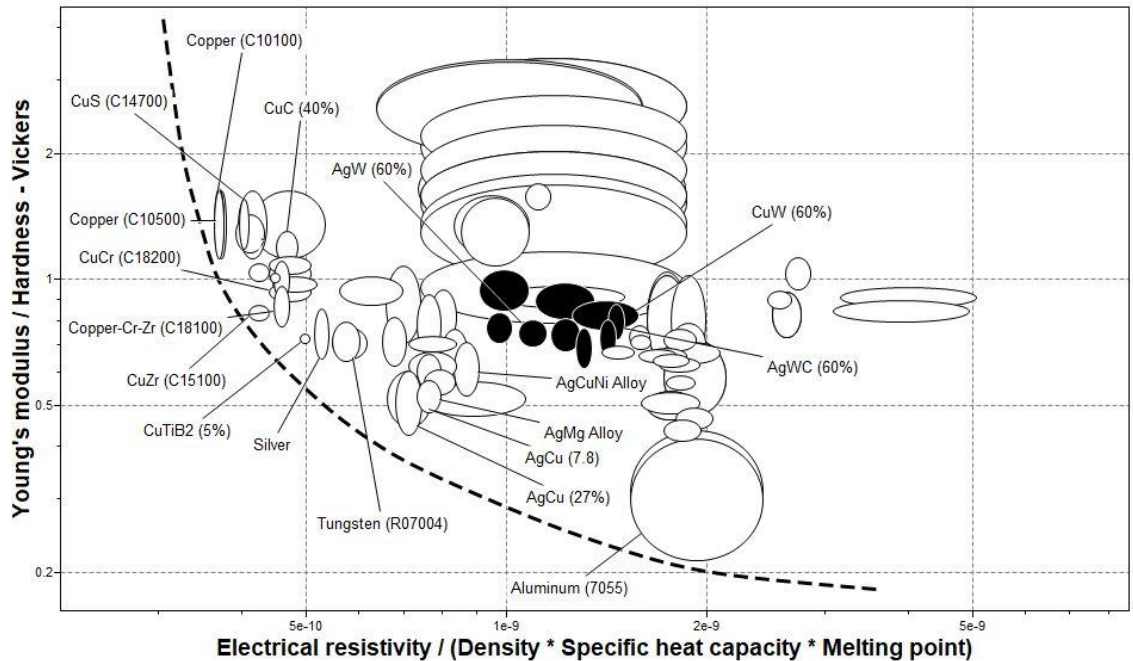


Figure 18 - Tradeoff plot for minimizing wear damage vs minimizing overheating

5.3.3 Materials Database

The material property charts are created using the CES Edupack Level 3 database. The Level 3 database consists of materials that cover the major engineering material families (metals, ceramics, glasses, polymers, elastomers and hybrids) so new or unlikely opportunities are not overlooked. However, the database does not contain some contact materials such as AgWC, AgW, and CuW, which are currently used as electrical contacts for conventional circuit breakers and vacuum interrupters. An analysis of contact materials for FMS would not be complete without including these materials. The materials properties such as resistivity, density and hardness are available by manufacturer datasheets [104]. These materials are manually added to CES for a more complete analysis.

This results in a database of about 4000 materials. To further reduce the subset, some reasonable assumptions about the material properties are made which are added as limit stages. These are:

1. The material has a solid bulk form, which includes plates, bars, rods, forging, casting, extrusion and molding.
2. Electrical Resistivity $< 10 \mu\Omega\cdot\text{cm}$ (Resistivity of Iron, which is not a good contact material due to low electrical conductivity)
3. Hardness > 100 Vickers
4. Thermal conductivity $> 173 \text{ W/mK}$ (λ of Tungsten, which is also not a good contact material due to poor thermal conductivity)

This limits the subset of materials to 95, which is a much more manageable number.

5.3.4 *Material Ranking*

The ranking of the materials can be accomplished by weighing the relative performance of each material index shown:

$$W_i = w_i \frac{(M_i)_{\min}}{M_i} \quad (20)$$

where w_i is a weight factors which sum up to 1, M_i is the material index value, and $(M_i)_{\min}$ is the minimum material index value of the materials that pass the screening

stage. This results in two weighted values W_i for each of the selected materials. The summation of the two weighted values is the overall performance P of each material candidate:

$$P = \sum W_i \quad (21)$$

The weight factors w_1 and w_2 correspond to M_2 and M_3 respectively. The weight factors are selected based on perceived importance of each material index to the performance of electrical contacts of FMS. Since there are no commercially available FMS, the overall performance is used to rank the material candidates to develop a list of candidates to be pursued further with the understanding that the candidates are based on the current knowledge of operating conditions of FMS and that they may change as knowledge improves.

Table 4 shows the materials ranked from high to low based on each material index. The purpose of this table is to gain more insight into different materials that can be used as electrical contacts based on relative weights given to different objectives. For each of the representative candidates listed in Table II several alloys, heat treatments and mechanical processing would be used to refine the selection for each class of material. For example, over a dozen different types copper pass the screening process. However, the purpose of this exercise was is to establish a baseline of different material candidates for relative comparison. For this reason, the candidates are listed in Table II with the understanding that a wide range of properties may be obtained from alloying, heat treatment, or work hardening to meet more specific needs that are explored in the fourth step, documentation.

Therefore, variation of the same material such as Copper 10500, Copper 10200 have all been represented by Cu, and CuW (70% Cu), CuW (60% Cu), CuW (50% Cu) have all been represented by CuW.

Table 4 – Material Ranking based on each objective

Objective (Minimize)	Metric	Material Ranking (High to Low)
Power Loss	ρ_c	Ag, Cu, CuTe, CuS, AgCu, CuC, CuZr, CuCr
Wear	$\frac{E}{H}$	Al, AgCu, Ag, CuPd, AgMg, AgCuNi, CuBeCo, Ag-MgO-NiO
Overheating	$\frac{\rho_c}{\rho C_p T_{melt}}$	Cu, CuTe, CuS, CuZr, CuTr, CuTiB2, CuCd, CuC

The table shows that if minimizing power loss is the main objective, then materials such as Ag, Cu and silver and copper based alloys are the most suitable materials. If minimizing wear is the main objective, then aluminum, silver and silver-based alloys are more suitable. If minimizing overheating is the main objective, then copper and copper-based alloys are most suitable.

In this dissertation, the material ranking is shown for three cases. Minimizing wear and overheating are given equal importance in the first case, minimizing wear is given higher relative importance in the second case and lower relative importance in the third case, and what is expected to be the most realistic case.

Case 1: $w_1 = 0.5, w_2 = 0.5$

Table 5 shows the performance index of the highest ranked materials. Copper, aluminum, copper-based alloys and silver have the highest performance index. This is

likely not a realistic representation of relative performance of performance indices and is only shown for the purpose of illustration of the ranking procedure.

Table 5 – Weighted material ranking for case 1

Material	M_2^*	M_3 ($\mu\Omega \cdot \text{cm} \cdot J^{-1} kg^{-1} m^3$)	P
Cu	1.38	3.69×10^{-10}	0.614
Al	0.3155	1.97×10^{-9}	0.593
CuTiB ₂	0.726	4.975×10^{-10}	0.588
CuZr	1.042	4.24×10^{-10}	0.586
CuCrZr	0.8715	4.59×10^{-10}	0.582
CuS	1.37	4.025×10^{-10}	0.573
AgCu	0.5165	7.12×10^{-10}	0.564
Ag (99.9% Purity)	0.571	5.27×10^{-10}	0.56

* M_2 has no units shown in the table as it contains hardness H which is measured in the Vickers Scale (HV 10)

Case 2: $w_1 = 0.8, w_2 = 0.2$

Table 6 - Weighted material ranking for case 2

Material	M_2^*	M_3 ($\mu\Omega \cdot \text{cm} \cdot J^{-1} kg^{-1} m^3$)	P
Al	0.3155	1.97×10^{-9}	0.837
Ag (Coin Silver)	0.5275	7.14×10^{-10}	0.581
AgMg	0.531	7.65×10^{-10}	0.572
CuPd	0.524	9.01×10^{-10}	0.563
CuTiB ₂	0.726	4.975×10^{-10}	0.496
AgCuNi	0.6125	8.7×10^{-10}	0.492
W	0.7085	5.81×10^{-10}	0.483
CuZr	1.042	4.24×10^{-10}	0.476

* M_2 has no units shown in the table as it contains hardness H which is measured in the Vickers Scale (HV 10)

Table 6 shows the performance index of the highest ranked materials. Aluminum has the highest performance index followed by silver and copper-based alloys and tungsten. If

minimizing wear in the contacts of the FMS is very high priority, then these materials would be most suitable as electrical contacts.

Case 3: $w_1 = 0.2, w_2 = 0.8$

While studies have shown higher fretting wear at lower contact force and elevated temperatures, the effect of current load on fretting is not clear. While some studies have shown that the onset of fretting is delayed by increasing current load, the currents in these experiments less than 3A [105, 106], which is too low to increase temperature of the contacts. At this time, it is unclear how a current load of a few hundred amperes or more affects fretting wear. However, materials with a high M_3 are more resistant to surface damage caused by elevated temperatures. So we can assume a lower weight factor for M_2 than M_3 . This is considered to be the most realistic case based on current knowledge. Table 7 shows the performance index of the highest ranked materials. Copper and copper-based compounds and alloys have the best performance index. If minimizing overheating contacts of the FMS (and resistivity) is very high priority, then these materials would be most suitable as electrical contacts.

5.4 Discussion

The tradeoff plot shows that there is no materials available in the optimum region that meets all the objectives. Silver and copper-based materials were found to be more suitable materials than commercially available metal matrix composites that were added to the database. This can be explained by the fact that electrical contacts of FMS have different requirements than conventional circuit breakers and switches. The contact

materials were ranked based on best performance for each objective. The selection of the contact material would depend on relative weight assigned to each of these objectives.

Table 7 - Weighted material ranking for case 3

Material	M_2^*	M_3 ($\mu\Omega \cdot \text{cm} \cdot J^{-1} \text{kg}^{-1} \text{m}^3$)	P
Cu	1.38	3.69×10^{-10}	0.845
CuS	1.37	4.025×10^{-10}	0.779
CuZr	1.042	4.24×10^{-10}	0.771
CuTe	1.295	4.12×10^{-10}	0.765
CuTiB ₂	0.726	4.975×10^{-10}	0.719
CuCrZr	0.8715	4.59×10^{-10}	0.715
CuCr	0.9365	4.7351×10^{-10}	0.691
CuC	1.2	4.675×10^{-10}	0.684

* M_2 has no units shown in the table as it contains hardness H which is measured in the Vickers Scale (HV 10)

Due to the large number of materials and varied tests required to test each objective, it is not possible to experimentally validate the material ranking for all the top ranked materials. However, experimental results in prior literature can be used to validate the ranking of materials. According to [38], the materials with lowest contact resistance are Au, Ag, AuPd, Cu and Cu alloys. However, Au and AgPd are screened out by the Ashby method due to low hardness. As a result, the top ranked materials for minimizing power loss in Table 4 fit well with the results from [38]. Ref. [39] shows that worn volume after fretting is lower in base metals than alloys due to faster oxidation of base metals. This tracks well with Table 6 which has Al and Ag ranked the highest. Ref. [40] shows that fretting wear is lower in Al compared to Cu at low oscillation frequencies (0.33 Hz) and contact forces (2 – 10 N). This could explain the absence of Cu among the top ranked materials in Table 6. Refs. [41] and [42] show that fretting wear in such copper alloys as

CuZr and CuPd is lower than that in pure Cu due to the higher hardness of copper alloys, which is also reflected in Table 6. There is prior work on the comparative performance of overheating/welding under short circuit of silver and copper materials under identical conditions. However, Refs. [43] and [17] show that silver and copper have higher resistance to overheating than their alloys and metal based compounds respectively. As the specific heat capacity of copper based materials are higher than silver based materials [35], silver based materials heat up quickly and are more susceptible to overheating. That explains why Table 7 is dominated by copper-based materials.

In summary, the ranking of materials in Tables 5-7 is broadly in agreement with experimental results. However, experimental data on every single material in the aforementioned tables cannot be found in literature. The broad agreement of experimental results with the material ranking from the Ashby method indicates that the top ranked materials must be investigated further with tests under identical conditions to find the most suitable contact material.

5.5 Summary

The HCB is designed to limit fault currents and energy absorbed in DC power systems. This is accomplished by having nominal current flow through the FMS and commutating the fault current to the parallel solid-state branch. The contacts of FMS must carry high continuous current with low power losses and must resist wear due to fretting, impact and Joule heating of contacts. The Ashby method is used to systematically identify the best-suited contact materials by translating the requirements of contact materials into

objectives and constraints and deriving material indices for each objective. CES Edupack was used to filter materials by applying constraints and rank materials using objectives. Commercially available metal matrix composite contact materials that were not in the CES database were added to make the analysis more thorough.

The results show that aluminum, silver and copper-based materials are the best materials if minimizing wear has high priority. Copper, aluminum and copper-based materials are the best materials if minimizing wear and overheating have equal priority. Copper-based materials are the best materials if minimizing overheating (and power loss) has a high priority. Copper-based materials rank highly in all the cases shown, and the top eight materials in the most realistic case are all copper-based. Therefore, copper-based materials are more suitable as FMS contacts than silver based materials and any other material considered in this study. The top ranked materials must be investigated further by seeking further documentation of availability, pricing and conducting field tests under identical conditions to identify the most suitable material amongst them.

The analysis assumed that the dimensionless wear coefficient will have a minimal effect on the suitability to FMS for the top candidate materials. This needs to be validated by experimentally determining K for the top candidate materials. Also, the analysis assumed that the pair of contacts are made of the same materials. Commercial circuit breakers generally use contact pairs with the same materials so there is insufficient information on performance of dissimilar material contacts. However, there could be advantages to having contacts made of dissimilar materials as they have lower tendency to stick and could reduce wear.

CHAPTER 6. ELECTRICAL CONTACT GEOMETRY

6.1 Motivation

The electrical contacts of the FMS should have a contact geometry that results in nearly uniform electric field (no field enhancement) to minimize the risk of electric breakdown when the contacts are open. Also, the contacts should have low power losses, which requires the contacts to have low bulk and constriction resistance. Uniform field geometries such as Bruce and Rogowski, which are used to make electrodes for applications that require uniform electric fields and Ernst and Chang profiles, which were developed to produce uniform electric field to obtain glow discharge in TE gas lasers, are investigated as potential contact geometries. The relative performance of these optimized geometries is compared w.r.t. electric field between the open contacts and contact resistance of closed contacts.

6.2 Optimized Contact Geometries

The mathematical functions that describe Bruce, Rogowski, Ernst and Chang geometries are shown below. All the geometries are shown in the half-plane. The three-dimensional contact geometry can be obtained by revolving this half plane around its z-axis by 360 degrees.

6.2.1 Rogowski Geometry

The Rogowski geometry has two sections: an exponential and a circular section that make a smooth transition. The geometry was derived by calculating the electric field associated with a flat plane above and infinite ground plane. The exponential section of the geometry is defined by the following set of parametric equations:

$$x = \frac{A_r}{\pi} (\phi + e^\phi \cos\psi) \quad y = \frac{A_r}{\pi} (\psi + e^\phi \sin\psi) \quad (22)$$

where ϕ is the electrostatic line of force, ψ is the equipotential surface and A_r is the distance separating the flat plane from the ground plane. This can be interpreted to be the distance of separation between the contacts and the Rogowski geometry and can be drawn for any given distance of separation. The transition between circular and exponential section takes place at $\phi = 0$. The circular section ends at the point where the slope becomes vertical. The computer program written in MATLAB to generate the geometry can identify the end point.

6.2.2 Bruce Geometry

The Bruce geometry has three sections: a circular section, a sinusoidal section, and a plane section. To make a Bruce contact, the plane section is eliminated and only the sinusoidal section and a portion of the circular section are adopted. Starting from a sinusoidal curve, the contact geometry converts to a circular curve until its slope is 90°.

$$y = -R_e \sin\left(\frac{x}{x_0} \frac{\pi}{2}\right) \quad (23)$$

To ensure smooth transition between circular and sinusoidal sections, R_e and X_0 are given by

$$X_0 = \frac{A_B}{\cos\alpha} \quad R_e = \frac{2}{\pi} X_0 \tan\alpha \quad (24)$$

where α is the characteristic angle of the sinusoidal section. A_B is the radial distance beyond which the Bruce section extends before meeting the circular section. It is assumed to have a fixed value (0.5 in the example in Section 3.2.2)

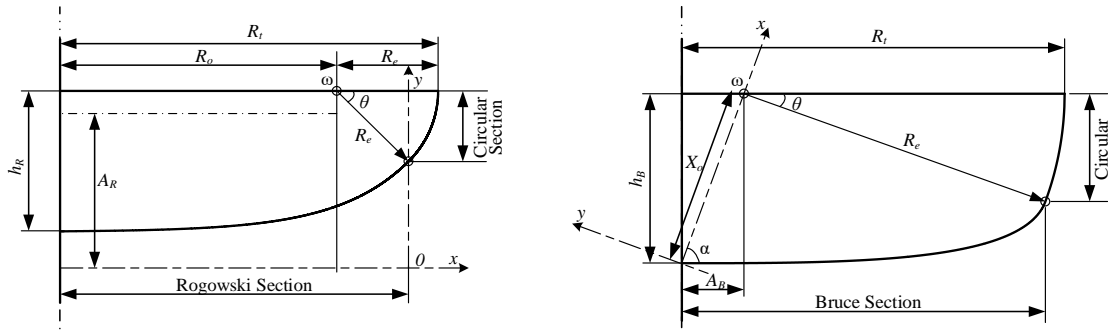


Figure 19– Rogowski Geometry (left) and Bruce Geometry (right) [63]

6.2.3 Chang Geometry

To construct the Chang geometry, two complex planes $z = x + iy$ and $W(z) = U + iV$ are defined where U is the flux function and V is the potential function. The analytical function is given by the equation.

$$z = W + K \sinh(W) \quad (25)$$

where K is a constant that can be chosen arbitrarily and a different curve is generated for each value of K . The corresponding flux and potential function in the z -plane are given by the equations

$$x = U + K \cos(V) \sinh(U) \quad y = V + K \sin(V) \cosh(U) \quad (26)$$

To construct the geometry, the value of V is selected to be $\frac{\pi}{2} + \theta$, where θ is a variable and the values of x and y are calculated by sweeping the variable U from 0 to a point where the slope of the curve becomes vertical. So the Chang geometry is controlled by 2 parameters: θ and K and does not depend on the distance of separation between the contacts. The Chang geometry results in more compact contacts than Bruce or Rogowski geometry.

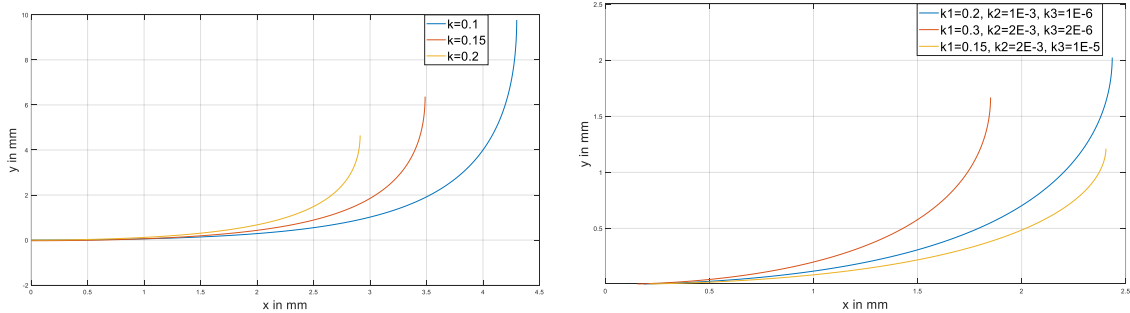


Figure 20 – Chang Geometry (left) and Ernst Geometry (right)

6.2.4 Ernst Geometry

The Ernst geometry results in a more compact geometry than the Chang geometry.

The analytical function is given by

$$z = W + k_0 \sinh(W) + k_1 \sinh(2W) + k_2 \sinh(3W) \quad (27)$$

where k_0, k_1 and k_2 are constants chosen arbitrarily and z and W are two complex planes similar to the Chang geometry. The corresponding flux and potential function in the z plane are given by the equations

$$x = U + k_0 \cos(V) \sinh(U) + k_1 \cos(2V) \sinh(2U) + k_2 \cos(3V) \sinh(3U) \quad (28)$$

$$y = V + k_1 \sin(V) \cosh(U) + k_2 \sin(2V) \cosh(2U) + k_2 \sin(3V) \cosh(3U) \quad (29)$$

The geometry is more compact than Chang but harder to construct as the variables are chosen arbitrarily and the wrong combination of variables make the geometry go out of proportion.

6.3 Electric Field Analysis

Electric breakdown in vacuum can take place either due to field emission or thermionic emission. The former causes electrostatically induced electrons to be emitted from the surface and the latter causes thermally charge carriers to flow over a potential barrier. While both field and thermionic emission can take place between the open contacts of FMS, only field emission is affected by the magnitude of the electric field on the surface of the electrodes. High electric field can result from contaminants on the contact surface or change in the structure of the contacts due to deformation, friction, and wear, experienced by the contacts during the operation of FMS. A geometry that minimizes the electric field in the gap between the contacts can reduce the possibility of a breakdown when the contacts are open. The electric field is modelled using a finite element model with 0.5 mm

separation between the contacts for all geometries, which is the same contact separation as the FMS prototype in Figure 3. However, the electric field analysis should be independent of the contact separation. All contacts have a circular base with radius of 5 mm. Since the electrical contacts are symmetrical in two axes, a 2D axisymmetric model is used. The medium between the contacts is vacuum. The top contact is given a potential of 1 V and the bottom contact is grounded. The normalized electric field, i.e. the electric field vector normal to the surface, is plotted along the surface of the 1 V contact. The maximum electric field along the surface of the contact is tabulated. If the electric field is uniform, the normalized electric field will have a maximum value of 2 V/mm.

6.3.1 Spherical, Elliptical and Flat Geometries

Figure 21 shows the variation of normalized electric field along the surface of the contact for circular, elliptical and flat contacts. It can be seen that elliptical and flat geometries have lower electric field than circular geometry at the centre ($r = 0$ mm). On the other end of the spectrum, flat contacts have high electric field at the edges of the contact, which make them unsuitable as contacts of FMS. The peak electric field along the contact surface for these geometries are shown in Table 8.

Table 8 - Peak Electric Field of Spherical, Flat and Elliptical Contacts (Radius = 5 mm)

Contact Geometry	Peak Electric Field (V/mm)
Spherical	2.0685
Flat	2.7577
Elliptical ($h = 2$ mm)	2.0271
Elliptical ($h = 3$ mm)	2.0406
Elliptical ($h = 4$ mm)	2.0544

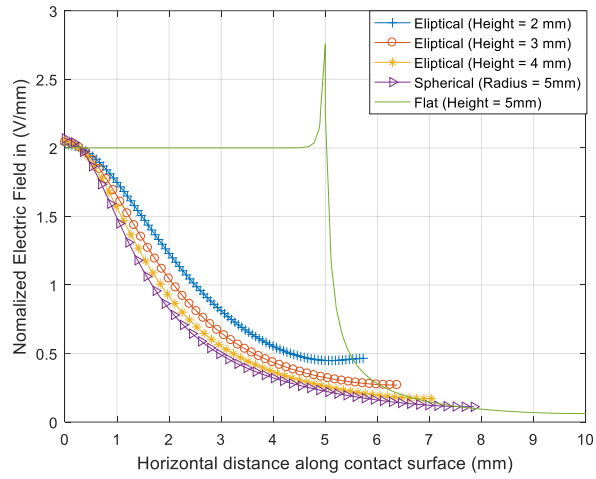


Figure 21 - Variation of Normalized Electric Field along surface for Spherical, Flat and Elliptical geometries.

6.3.2 Bruce and Rogowski Geometries

Figure 22 shows the variation of normalized electric field along the surface of the contact for different Rogowski geometries. Rogowski geometries with $\phi = 270^\circ$, 360° , 450° and 540° have a lower peak electric field than spherical geometry. The peak electric field values are shown in Table 9.

Table 9 - Peak Electric Field of Rogowski Contacts (Radius = 5 mm)

Contact Geometry	Peak Electric Field (V/mm)
$\phi = 180^\circ$	2.1790
$\phi = 270^\circ$	2.0380
$\phi = 360^\circ$	2.0081
$\phi = 450^\circ$	2.0017
$\phi = 540^\circ$	2.0000

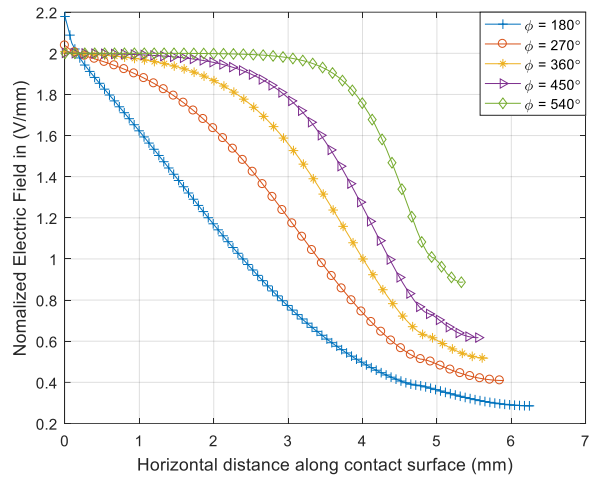


Figure 22 - Variation of normalized electric field along surface for different Rogowski geometries.

Figure 23 shows the variation of normalized electric field along the surface of the contact for different Bruce geometries. All the Bruce geometries shown have a lower peak electric field than spherical geometry. The peak electric field values are shown in Table 10.

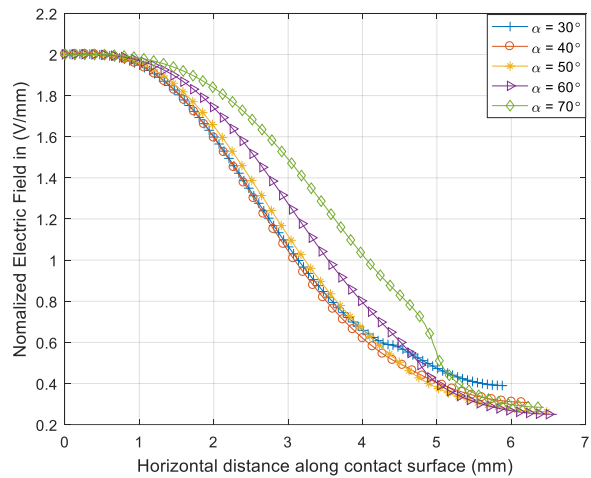


Figure 23 - Variation of normalized electric field along surface for different Bruce geometries.

Table 10 - Peak Electric Field of Bruce Contacts (Radius = 5 mm)

Contact Geometry	Peak Electric Field (V/mm)
$\alpha = 30^\circ$	2.0023
$\alpha = 40^\circ$	2.0023
$\alpha = 50^\circ$	2.0019
$\alpha = 60^\circ$	2.0013
$\alpha = 70^\circ$	2.0007

6.3.3 Ernst and Chang Geometry

Figure 24 shows the variation of normalized electric field along the surface of the contact for different Chang geometries. Although the electric field near the center of the geometry is uniform, field enhancement at the edges can lead to higher peak electric fields. Chang geometries with $k = 0.2, 0.3$ and 0.4 have a lower peak electric field than spherical geometry. The peak electric field values are shown in Table 11.

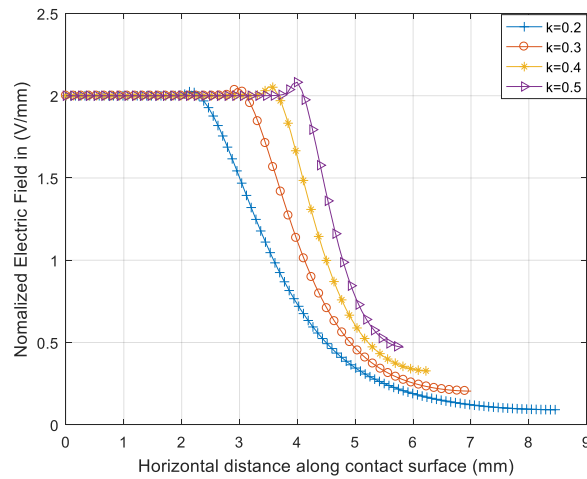


Figure 24 - Variation of normalized electric field along surface for different Chang geometries.

Table 11 - Peak Electric Field of Chang Contacts (Radius = 5 mm)

Contact Geometry	Peak Electric Field (V/mm)
$k = 0.2$	2.0276
$k = 0.3$	2.0438
$k = 0.4$	2.0535
$k = 0.5$	2.0821

Figure 25 shows the variation of normalized electric field along the surface of the contact for different Ernst geometries. Although the electric field near the center of the geometry is uniform, field enhancement at the edges can lead to higher peak electric fields. All the Ernst geometries shown in Table 1 have a lower peak electric field than spherical geometry.

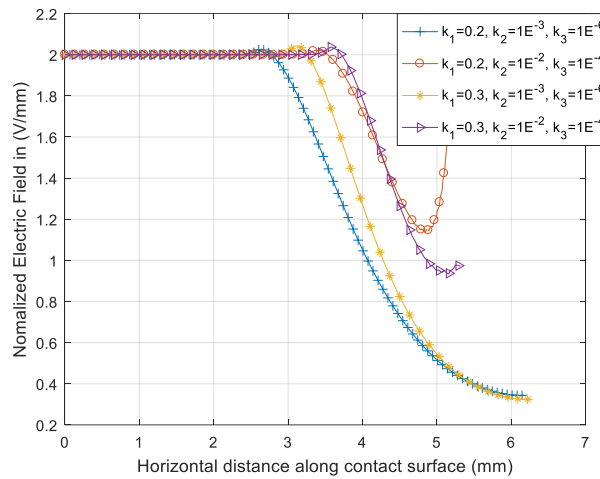


Figure 25 - Variation of normalized electric field along the surface for different k values

Figure 26 shows the comparison of the electric field along all the contact geometries mentioned in this dissertation. The highest electric field is located at the sharp edge of the cylindrical contact, which causes electric field enhancement. The lowest electric field is

along the surface of the Rogowski contact with $\phi = 540^\circ$. In general, optimized contact geometries have a more uniform electric field distribution. This leads to a lower peak normalized electric field compared to spherical and elliptical geometries, as shown in Table 13.

Table 12 - Peak Electric Field of Ernst Contacts (Radius = 5 mm)

Contact Geometry	Peak Electric Field (V/mm)
$k_1 = 0.2, k_2 = 10^{-3}, k_3 = 10^{-6}$	2.0271
$k_1 = 0.2, k_2 = 10^{-2}, k_3 = 10^{-4}$	2.0218
$k_1 = 0.3, k_2 = 10^{-3}, k_3 = 10^{-6}$	2.0432
$k_1 = 0.3, k_2 = 10^{-2}, k_3 = 10^{-4}$	2.0376

Table 13 – Peak electric field for different contact geometries

Contact Geometry	Peak Electric Field (V/mm)
Spherical	2.0685
Flat	2.7577
Elliptical ($h = 2.5$ mm)	2.0271
Rogowski ($\phi = 540^\circ$)	2.0000
Bruce ($\alpha = 70^\circ$)	2.0007
Chang (k=0.2)	2.0276
Ernst ($k_1 = 0.2, k_2 = 10^{-3}, k_3 = 10^{-6}$)	2.0271

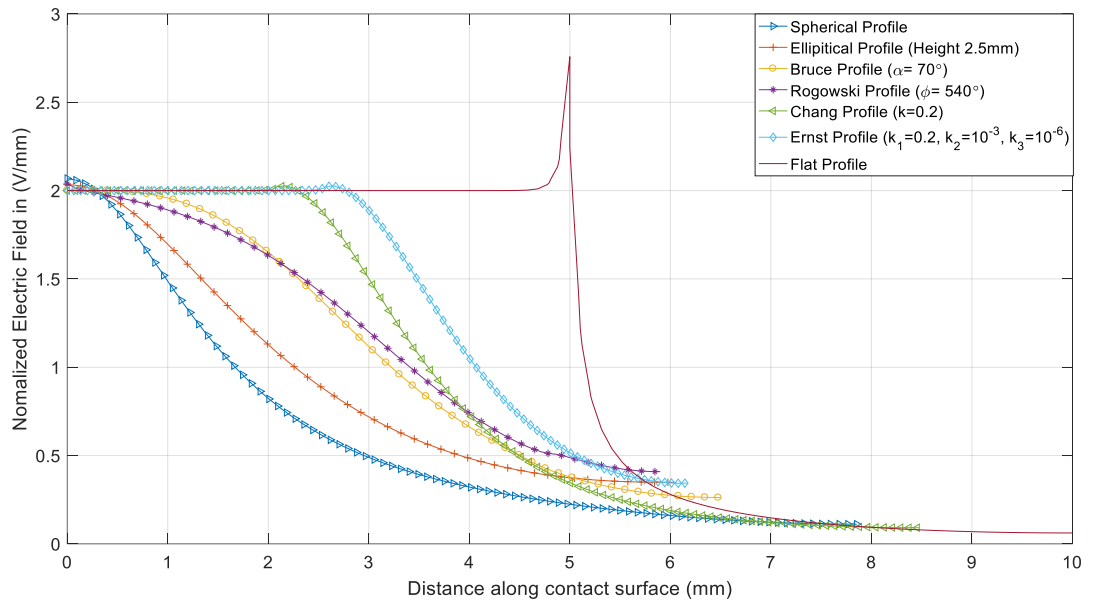


Figure 26 - Variation of normalized electric field along surface for different geometries.

6.4 Experimental Validation

The contact experiment setup is built to measure the resistance of contacts with different geometries. The setup can also be used to conduct experiments on thermal performance of different contact materials as a function of contact force and short circuit currents.

6.4.1 Experiment Setup Description

The setup consists of a six-way cross, which is a spherical chamber with ConFlat vacuum flanges in a cube arrangement (top, bottom, front, back, left and right). On two opposite flanges, a feedthrough and a linear motion actuator are attached, respectively. Electrical contacts are bolted to the copper feedthrough and a copper rod, which is attached

to the linear motion actuator through a load cell and a vibration mount. The force between the contacts is adjusted by manually rotating the actuator, which will press one contact onto the other. The load cell will measure the force between the contacts and the vibration mount is used to reduce the spring constant of the system. This allows the force between the contacts to be adjusted with an accuracy of ± 1 N. The measurements taken inside the chamber, such as force and the electrical contact resistance, are read outside the chamber through a multi-pin feedthrough. The chamber is evacuated using a pump and the measurements are taken at a maximum pressure of 10^{-3} mbar.

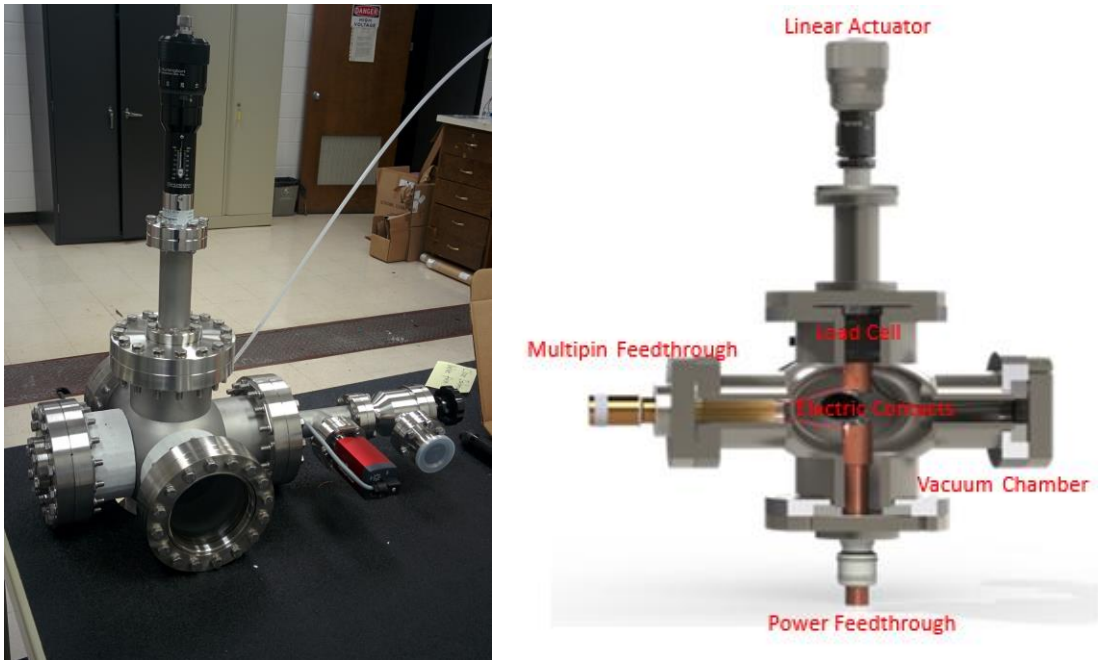


Figure 27 - Picture of the Contact Experiment Setup (left); CAD rendering of contact experiment with parts labelled (right)

The design of contacts used in the experiment is shown in Figure 29. All the contacts are made of high-purity 101 copper and are machined in a CNC mill. Copper is chosen due to its high conductivity and relative ease of obtaining the material (compared

to more common contact materials like AgWC) for experimental purposes. All the contacts have a circular base with radius 5 mm. They are mounted on a 4 mm thick circular plate of 25 mm diameter. The plate features countersunk holes that allow the contact to be bolted to the feedthroughs without the bolt heads protruding (Fig. 29). All the tested contacts have similar volume with 11% difference in volume between contact with the highest and lowest volume. Thus, the difference in contact resistance between different geometries is mostly due to constriction resistance and not bulk resistance.



Figure 28 - Contact bolted to linear motion actuator

Direct current is passed through the contacts using a fully programmable lab power supply (Magna Power TS Series). The copper conductors, to which the contacts are bolted, have a hole through which banana plugs are inserted. The voltage drop between these terminals divided by the current is considered the resistance of the contacts for this experiment. The contacts are cleaned to remove any contaminants on its surface. The resistance is measured at currents of 5, 10, 15, 20 and 25 A as a function of force by adjusting the force between the contacts from 5 N to 200 N. Since the currents are fairly low passed for a short duration (less than 1 minute), any effect on contact resistance due to Joule heating is minimized. Figure 30 shows the resistance of the contacts as a function of force for different contact geometries.

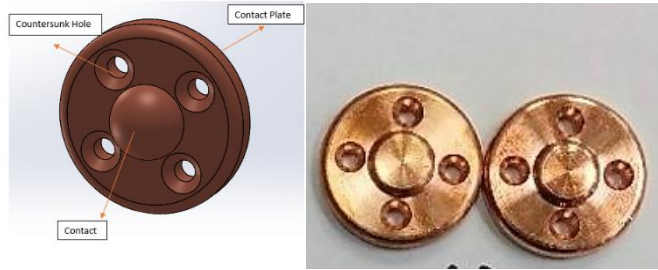


Figure 29 - CAD model of electrical contact with parts labelled (left); Machined Rogowski contacts ($\phi = 3\pi$) (right).

6.4.2 Contact Experiment Results

As the contacts are made of the same piece of copper and machined on the same mill, the surface properties of the contacts are similar. The average roughness of contacts of all the geometries were found to be between $0.4 - 0.6 \mu\text{m}$. The contact resistance has 3 components: bulk resistance, constriction resistance and film resistance [107]. The contact surfaces have thin films on its surface which include contaminants, adsorbed gases, oxide layers and work hardened layer – all of which have higher resistance than metal substrate. At low loads, the film resistance will dominate as the oxide films, that have higher resistance than copper, are in contact. As the load is increased, the thin films are destroyed and the bulk of the currents flow through the highest asperities, or a-spots, on the surface of the contacts. This resistance, known as the constriction resistance, dominates when the load is increases as the number of a-spots increases. At higher loads, more and more a-spots come into contact and deform plastically so the bulk resistance of the contacts will dominate as the real area of contact is very close to the nominal area of contact. In Figure 29, the difference in volume between different geometries is 11% between the geometry with highest volume (flat) and lowest volume (Ernst). Thus, the difference in contact

resistance between different geometries cannot be due to the difference in bulk resistance. Figure 30 shows that spherical contacts have the highest resistance and flat contacts have the lowest resistance. However, flat contacts have high electric field at their edges, which make them unsuitable as contacts of the FMS. Optimized contact geometries such as Bruce, Rogowski, Ernst and Chang have low contact resistance as well as uniform electric field, which make them very suitable as contacts of FMS.

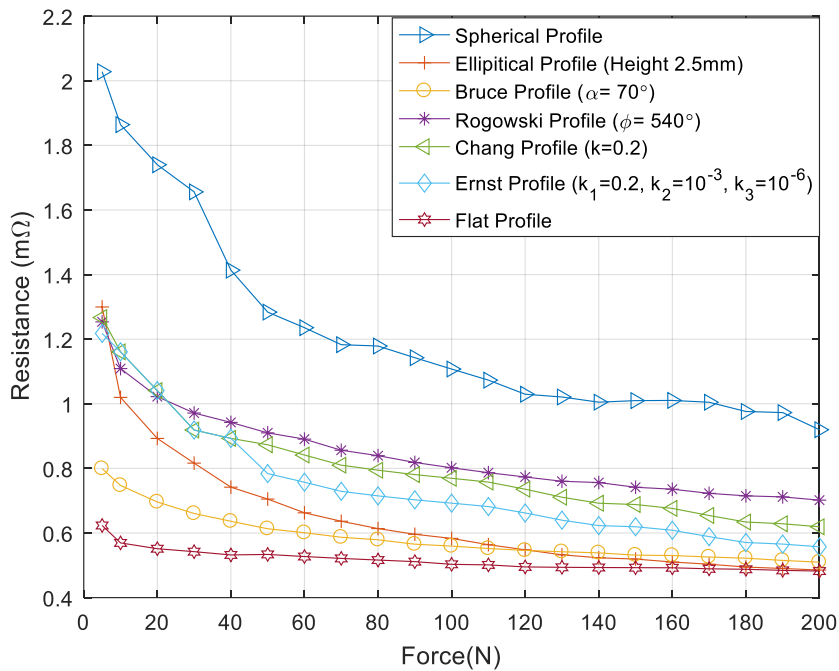


Figure 30 - Contact Resistance vs Force for different contact geometries.

6.5 Summary

The electrical contacts of FMS should have a geometry that results in low power loss when closed and uniform electric field when open. Different contact geometries such as Elliptical, Bruce, Rogowski, Ernst and Chang are explored to be used in proposed FMS.

Finite element models show that optimized contact geometries have more uniform electric field than spherical geometry. Experimental results show that optimized geometries have up to 40% lower contact resistance than spherical geometry.

CHAPTER 7. IMPACT OF FRETTING WEAR

7.1 Motivation

The lower force between the contact pairs of APA FMS makes them more susceptible to fretting wear. The contacts are expected to be exposed to repeated relative surface motion between their surfaces in applications such as electric ships and aircraft. The fretting scar can change the surface roughness of the contacts. The increase in surface roughness can reduce the breakdown voltage of the FMS as the contact separation is very low. This chapter explores the impact of fretting wear but conducting fretting experiments on a ball and flat tribometer. The surface roughness parameters of the contacts after fretting are measured and used to recreate surfaces in a finite element model to calculate the new breakdown voltage.

7.2 Experiment Setup Description

There are no experimental data for fretting available for piezoelectric FMS, As a result, the fretting scars are generated using a ball-on-flat reciprocating motion tribometer shown in Figure 31, which incorporates three main units used for driving, measuring and loading purposes. The drive unit consists of a DC motor-driven spindle and a moving table, which are connected using a crank mechanism with adjustable eccentricity to convert the rotational motion of the spindle into the reciprocating linear motion of the table. The table holds the copper plate sample and oscillates with adjustable frequency of up to 10 Hz with

a displacement amplitude of up to 80 μm . The measuring unit consists of a hinged balanced lever incorporating the upper sample holder, a force transducer and a proximity probe.

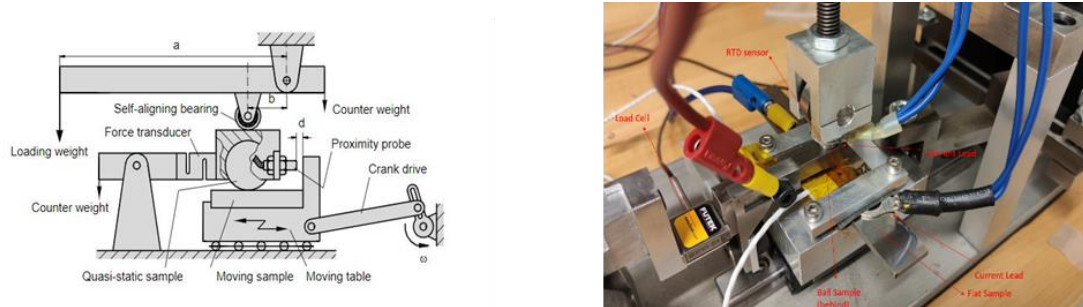


Figure 31 - Schematic of ball-on-flat reciprocating tribometer (left) [108], picture of the experiment with a protruding stainless steel flat sample and parts labelled (right)

A ball sample of 5 mm diameter is mounted in the holder. This is comparable to the size of the contacts in the FMS prototypes, which have a diameter of 10 mm [6] and between 5-10 mm [9], respectively. The loading unit consists of another hinged and balanced lever, where the applied dead load is amplified by a factor of four and is applied through a self-aligning bearing to the ball holder in order to press the stationary ball sample against the moving plate sample. To obtain information about the presence of wear debris in the contact zone, the electrical contact resistance of the interface is monitored using Ohm's law after passing a constant current through while measuring the voltage drop across the contact.

7.3 Contact Surface Analysis Experiment

The experiments were conducted using a 5 mm copper sphere and a cylindrical copper plate with 25.4 mm and 5 mm thickness. The surface properties of the copper plate

were measured prior to the experiments using an optical profiler. Fretting experiments were conducted with 9.8 Hz frequency for 6000 cycles at different regions of the copper plate, which is comparable to the frequency of between 0 – 10 Hz for fretting wear between connectors in aircraft and automobiles [100, 109]. A 500 g mass was applied at the end of the self-aligning bearing, leading to a contact force of 20 N between the ball and plate. The force is on the lower end of the contact force of the piezoelectric FMS prototypes, which is between 27 – 40 N. The experiment was repeated with a current of 0.18 A, 15 A, 30 A, and 50 A respectively, conducted from the copper ball to the plate. The experiment under 0.18 A represents the fretting under no load, as the current is small enough to avoid any joule heating, but high enough to continuously monitor the contact resistance during the experiment. After the experiment, the surface properties of the copper plate in the region subjected to fretting was measured after the experiments using the optical profiler. Due to the difficulty of holding and focusing the profiler lens on a small spot on the spherical surface, the surface properties of the ball are not measured. It is assumed that both the copper ball and plate will have similar surface properties after fretting since they are made of the same material.

As each run consists of 6000 cycles, any difference in the initial surface properties of the flat sample will not have a significant effect. Multiple runs conducted at the same current and force showed initially no significant differences between surface properties of fretting scars. The contact resistance was continuously measured as the fretting tests were conducted and they were similar for multiple runs. As a result, the surface properties are obtained from a single run of 6000 cycles as the likelihood of getting abnormal data is low.

Figure 32 shows the surface profile of the copper plate before and after the fretting experiments. The surface damage is greater as the applied current is increased due to the combination of Joule heating and fretting wear at higher currents. The damaged region consists of a depression in the middle accompanied by peaks at the edges of the fretting scar. The peaks can amplify the electric field between electrical contacts subjected to fretting wear. The surface parameters of the fretting scar are measured to study the extent of electric field amplification.

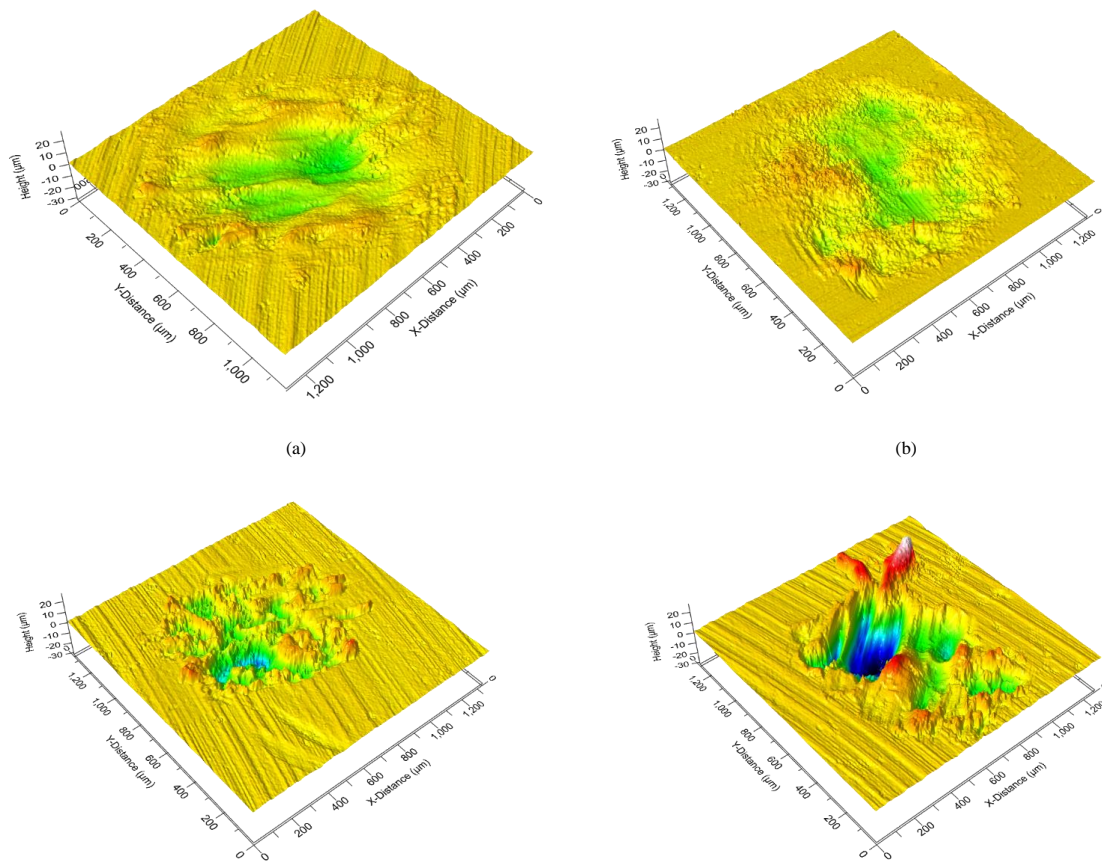


Figure 32 - Optical profile of copper plate after fretting at a) 0.18 A, b) 15 A, c) 30 A, d)

50 A

Table 14 shows the roughness average (S_a) and the root mean square surface slope (S_{dq}) of the damaged area. The roughness average increases with the applied current but S_{dq} , which gives an indication of how sharp the peaks and valleys are, do not show any relationship with the applied current. The electric field between contacts in the gap is enhanced by peaks on the contact surface above the mean plane of the contacts. The valleys do not contribute to increased electric field. As a result, S_a is calculated for points above the mean plane.

Table 14 – Surface parameters of the fretting spot above plane level

Load Current (A)	S_a (μm)	S_{dq}
Before Experiment	0.345	64.238
0.18 A (~No Load)	1.924	73.592
15 A	2.211	67.838
30 A	2.927	52.941
50 A	5.541	68.754

7.4 Surface Generation

To obtain electric field between the damaged regions while the electrical contacts are open, the surface profile measured after fretting experiments is recreated in a finite element package. There are several different ways to recreate the surface. The surface geometry can be almost exactly recreated by importing the optical profile into the FEM package. However, this would result in problems with resolution and computation time. The more commonly used method is to generate random surfaces based on extracted roughness parameters. The result of the FEM analysis would be the aggregation of results from multiple random surfaces. In this paper, a 2D FEA model is used to generate random curves

based on extracted roughness parameters for both the top and bottom contact. The electric field between the contacts is calculated using electrostatic field analysis.

According to [110], a random curve can be represented as a function of spatial frequencies and elementary waves as:

$$y = f(x) = \sum_{n=-N}^{n=N} a(n) (\cos(2\pi nx) + \phi(n)) \quad (30)$$

where x and y are spatial coordinates, m and n are spatial frequencies, $a(n)$ and $\phi(n)$ are amplitudes and phase angles, respectively. The phase angles $\phi(n)$ were randomly generated from a uniform distribution. To generate more natural looking surfaces, $a(n)$ was determined as a product between a normal distribution $g(n)$ and $h(n)$, where

$$h(n) = \frac{1}{n^{-\frac{b}{2}}} \quad (31)$$

where b is the spectral exponent and represents the decay of high frequencies. Eq. 1 was implemented as a parametric line that was scaled with the measured Ra from Table 14. The spectral exponent was set to $b = S_{dq} \frac{\pi}{360}$, from the measured surfaces. Similar methods have been used to generate rough surfaces in prior literature where the highest peak R_p is used to scale the random curve [111].

Due to its definition, the function $f(x,y)$ will be periodic. In order to get a natural-looking surface, we should “cut out” a suitably small portion by letting x and y vary between some limited values. While the size of the damaged region can be as large as 1 mm end-to-end, it is restricted to points on a 100 μm grid in the FEA model to reduce the

computation time. By setting N in Eq. 2 to 500, the fastest oscillation of the random curve is $2\ \mu\text{m}$. This results in a large number of peaks and valleys in the fretting damaged region, as observed in Figure 33.

7.5 Electrostatic Field Analysis

The FEA model consists of two randomly generated curves that represent the surfaces of the two contacts. The curves are generated from the extracted values of S_a and S_{dq} in Table 14 using eq. 1 and 2. Each contact is represented by a $125\ \mu\text{m}$ long curve with $100\ \mu\text{m}$ at the center representing the region damaged by fretting and $25\ \mu\text{m}$ at the edges, representing the surface of copper before fretting wear, as shown in Figure 33. The blue region represents the region around the contacts where the electric field is calculated. The size of the fretting spot is chosen to be $100\ \mu\text{m}$ to minimize the computation time of the FEA model. Increasing the length to the actual size of the fretting spot has very little effect ($< 3\%$ for $50\ \text{A}$) on the peak electric field.

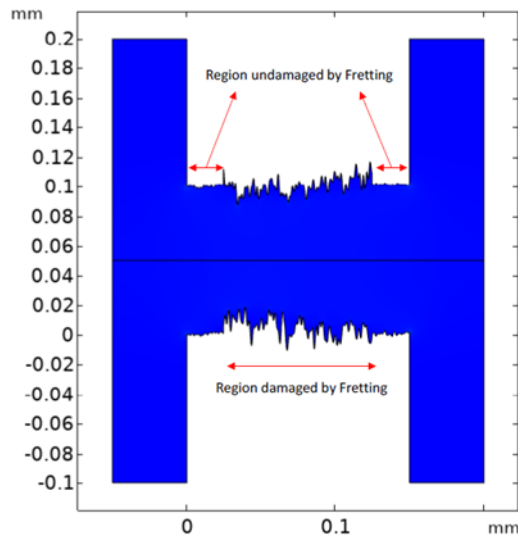


Figure 33 - Electrostatic field between curves representing surfaces separated by 100 μm after fretting wear at 30 A.

The top contact is given a potential of 1 V and the bottom contact is grounded. The normalized electric field, i.e. the electrostatic field vector normal to the surface, is plotted along the center of the contact gap. The maximum electric field along the horizontal line at the center of the contact gap is calculated. For each load current, the simulation is repeated ten times and the average electrostatic field in the gap is calculated.

Figure 34 shows the normalized electrostatic field along the line at the center of the gap for a gap distance of 50 μm and 100 μm , respectively. In general, the magnitude of the electrostatic field is greater after fretting wear under increasing currents. The electrostatic field is generally the highest around the center of the fretting scar. The field enhancement is less uniform at 50 μm gap as the effect of surface parameters are more pronounced.

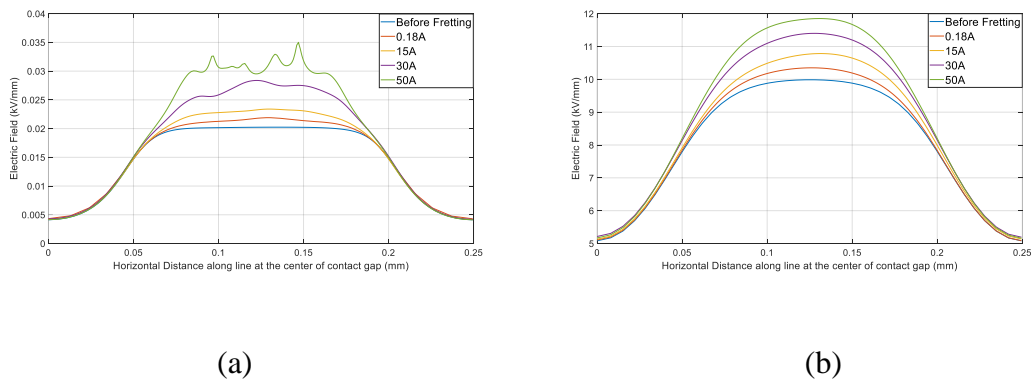


Figure 34 - Electrostatic field after fretting at the center of contact gap as a function of load current a) with 50 μm gap b) with 100 μm gap.

Table 15 shows the peak electrostatic field after fretting under various load currents for a contact gap of 50 μm and 100 μm , respectively. The peak electrostatic field after

fretting under 50 A is 1.73 and 1.19 times greater than the peak electric field before fretting for 50 μm and 100 μm , respectively. This would not have a great impact on electrostatic field on APA-based FMS where the contact gap is much larger. However, at currents closer to rated current, impact of fretting wear in APA-based FMS would need to be studied.

Table 15 - Peak electrostatic field

Load Current (A)	50 μm gap (kV/mm)	100 μm gap (kV/mm)
Before Experiment	0.0202	0.0100
0.18 A	0.0219	0.0104
15 A	0.0234	0.0108
30 A	0.0284	0.0114
50 A	0.0350	0.0119

7.6 Breakdown Voltage Estimation

The breakdown voltage between the contact surfaces after fretting wear can be predicted from the streamer breakdown criteria

$$\int_{\tau} \alpha_{\text{eff}}(E) = K = \ln(N_c) \quad (32)$$

where $\alpha_{\text{eff}}(E)$ is the field dependent effective ionization coefficient and K is the ionization constant and N_c is the number of electrons needed to create a self-propagating streamer head. The integration path of the streamer τ is assumed to follow the most critical path. $\alpha_{\text{eff}}(E)$ can be determined from the empirical fit functions [112].

$$\frac{\alpha_{\text{eff}}(E)}{p} = 1.6053 \left(\frac{E}{p} - 2.165 \right)^2 - 0.2873 \quad (33)$$

For $\frac{E}{p} < 7.94 \frac{\text{kV}}{\text{mm}\cdot\text{bar}}$ and

$$\frac{\alpha_{\text{eff}}(E)}{p} = 16.7766 \frac{E}{p} - 80.006 \quad (34)$$

For $\frac{E}{p} > 7.94 \frac{\text{kV}}{\text{mm}\cdot\text{bar}}$

There is no consensus around the value of K , which has been calculated experimentally for sphere-sphere electrodes in air with the gap in centimetre range to be between 9 – 18. The value of K depends on the atmospheric conditions (pressure, temperature, humidity), the order of magnitude of the contact gap and the geometry and roughness of the electrodes used in the experiments. Since the conditions of the experiments to determine K are not similar to the media of the FMS contacts, the value of K was determined via finite element models based on the fact that the dielectric strength of air is approximately 3 kV/mm. At a contact gap of 50 μm and 100 μm , this results in a breakdown voltage of 150 V and 300 V respectively.

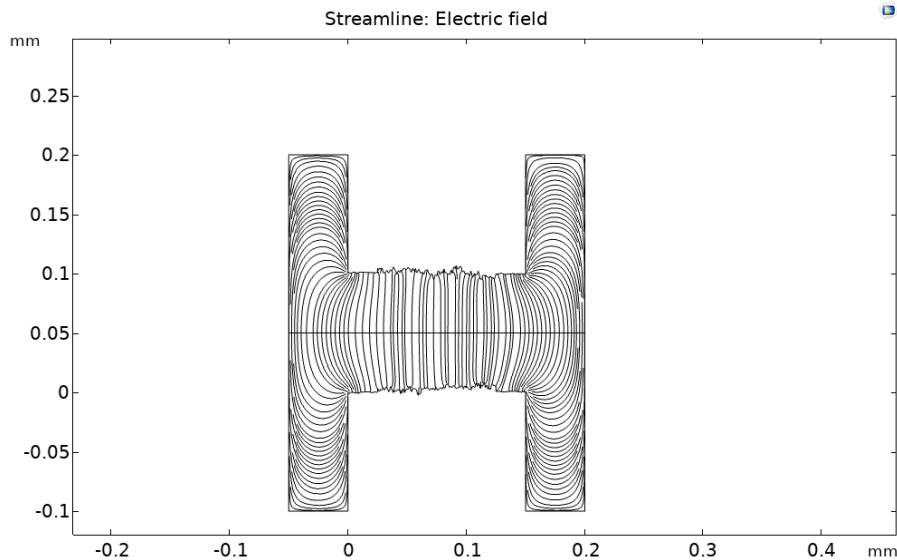
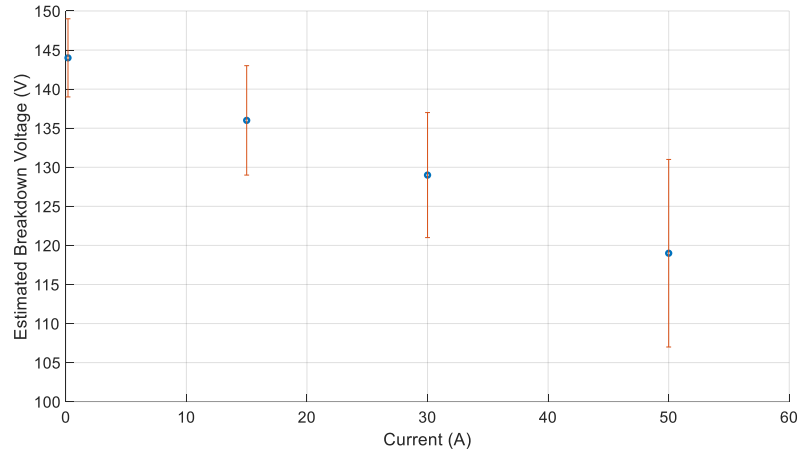


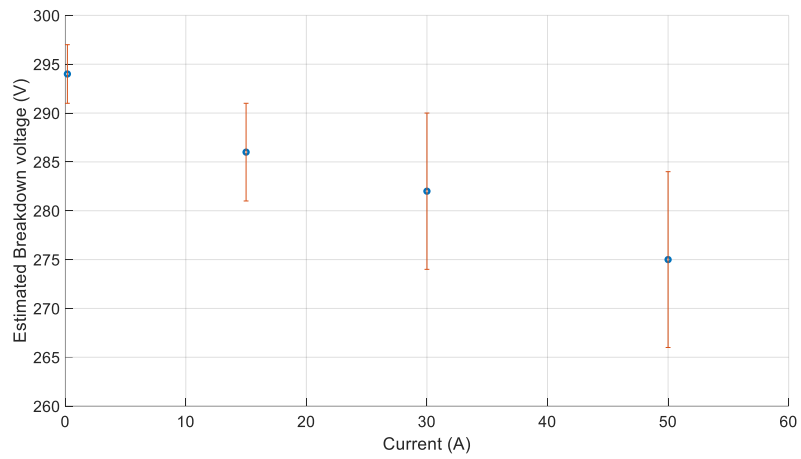
Figure 35 – E-field lines between top and bottom contact surfaces before fretting

The value of K is determined for the contact surfaces before the fretting experiment with the top contact given the voltage of 150 V and 300 V at a contact gap of 50 μm and 100 μm , and the bottom electrode grounded. The contact surfaces are randomly generated from the measure S_a and S_{dq} . Figure 35 shows the electric field lines between the contacts with a contact gap of 100 μm . Eqn 3 is calculated for the most critical field line, which prior literature has assumed to be a straight line between the center of the two contacts. In this dissertation, that value of K is calculated for 50 evenly spaced straight lines from one contact to another. The highest value of K is considered the ionization constant between those surfaces. A similar procedure is repeated for fretting surfaces generated as shown in section 7.4 for $I = 0.18\text{ A}$, 15 A, 30 A and 50 A where the value of K is calculated by sweeping the voltage of the top contact from $V = 0$ to 300 V. The voltage at which the calculated value of K exceeds the ionization constant is the breakdown voltage after fretting. The process is repeated for ten different randomly generated surfaces after fretting wear at each current level. Figures 36 (a) and (b) show the breakdown voltages obtained from these calculations for 50 μm and 100 μm gap, respectively.

The calculated breakdown voltage is lower when current at which the fretting wear takes place is higher. The relative reduction of breakdown voltage is greater at smaller contact gaps. The average breakdown voltage after fretting under 50 A is 8.33% lower at 100 μm contact gap. The average breakdown voltage after fretting under 50 A is 20.66% lower at 50 μm contact gap. As a result, piezoelectric FMS with low contact gaps must be designed by considering voltage derating due to fretting wear.



(a)



(b)

Figure 36 – Breakdown voltage vs. fretting current for a) 50 μm b) 100 μm contact gap

7.7 Summary

After performing experiments and simulations, the following conclusions have been made about the impact of fretting wear on the electric field in the contact gap:

It was observed that the average roughness after fretting increased with load current. At 50 A, the surface damage is more severe due to combination of Joule heating and fretting. The surfaces are recreated in a finite element package using average roughness and the root mean square surface slope. The peak electrostatic field in the contact cap increases after fretting wear and increases with load current. The peak electrostatic field is 1.73 and 1.19 times higher after fretting under 50 A than before fretting for 50 μm and 100 μm contact gaps, respectively. The combination of fretting and Joule heating exacerbates the surface damage causing a large increase in electric field. The electric field under rated currents of FMS could be higher as the impact of surface damage at a 600 A, the rating of the APA FMS, would be more severe. The breakdown voltage is estimated from the electrostatic field lines. The average breakdown voltage after fretting under 50 A is 8.33% lower and 20.66% lower for 100 μm and 50 μm contact gap, respectively.

The fretting experiments must be conducted for materials of higher hardness, which are more likely to be used as FMS contacts [83], to determine the roughness parameters as a function of load current. The value for the spectral exponent b was determined by trial and error and should be studied in more detail. It should be investigated if there is a more suitable parameter other than S_a for scaling the randomly generated surface. Finally, it would be interesting to expand the model into three dimensions and check if there are any variations to the calculated peak electric field versus load current. As the FMS is typically rated for several hundreds of amperes, the voltage derating due to fretting wear could be potentially greater at higher currents and needs to be studied further.

Therefore, the impact of fretting wear on the voltage rating of FMS must be a design consideration for piezoelectric FMS.

CHAPTER 8. DISSIMILAR CONTACT MATERIALS

8.1 Motivation

This chapter explores the opportunity of using dissimilar contact materials in a contact pair and the resulting performance improvements for the FMS. It is well known that similar materials have a higher chemical affinity towards each other than dissimilar materials. This results in a larger amount of material displaced due to wear between similar materials over dissimilar materials [113]. This idea is explored for electrical contacts of FMS by measuring the increase in contact resistance through the processes of fretting wear between similar and dissimilar materials.

Dissimilar materials, with different thermal conductivities and surface roughness, can also be used to control the flow of heat [74]. The current rating of piezoelectric FMS is limited by the maximum operating temperature of the piezoelectric actuator, which is around 100°C according to the manufacturers [76]. By directing the flow of heat away from the piezoelectric actuator, the current rating of the FMS can be improved. This idea is explored by finite element simulations and validation through experiments.

8.2 Fretting Wear

8.2.1 Experiment Description

The experiments were conducted on a ball-on-flat tribometer described in Figure 31. The experiments used 3D printed sterling silver $\text{Ag}_{92.5}\text{Cu}_{7.5}$ and copper ball and plate

samples. 3D printed samples are used due to the difficulty of machining 5 mm balls made of sterling silver. The samples are 3D printed by the manufacturer using lost wax casting technology. The surface properties of the plate sample measured prior to the experiments using an optical profiler. Fretting experiments were conducted with 9.8 Hz frequency for up to 25,000 cycles at different regions of the plate sample. A 500 g mass was applied at the end of the self-aligning bearing, leading to a contact force of 20 N between ball and plate. The experiment was repeated with a current of 0.18 A, 10 A, 20 A, and 30 A respectively,. The contact resistance between the ball and the plate is continuously monitored. It should be noted that the resistance measurement also includes the bulk resistance of the plate and ball in addition to the contact resistance. However, the contact resistance dominates the measured resistance. As a result, the ratio of the instantaneous resistance to the resistance at the beginning of fretting wear (R/R_0) is calculated. If (R/R_0) is greater than 10, then the contacts are considered to have failed due to fretting wear.

8.2.2 *Experiment Results*

Figure 37 shows the R/R_0 as a function of the number of cycles for sterling silver ball and copper plate samples. The experiment is conducted with a direct current of 10 A conducted from the ball to the plate. The contacts resistance increases with the number of cycles and the resistance ratio for four different runs seem to be similar. The average R/R_0 of four runs is calculated for all material combinations and current levels.

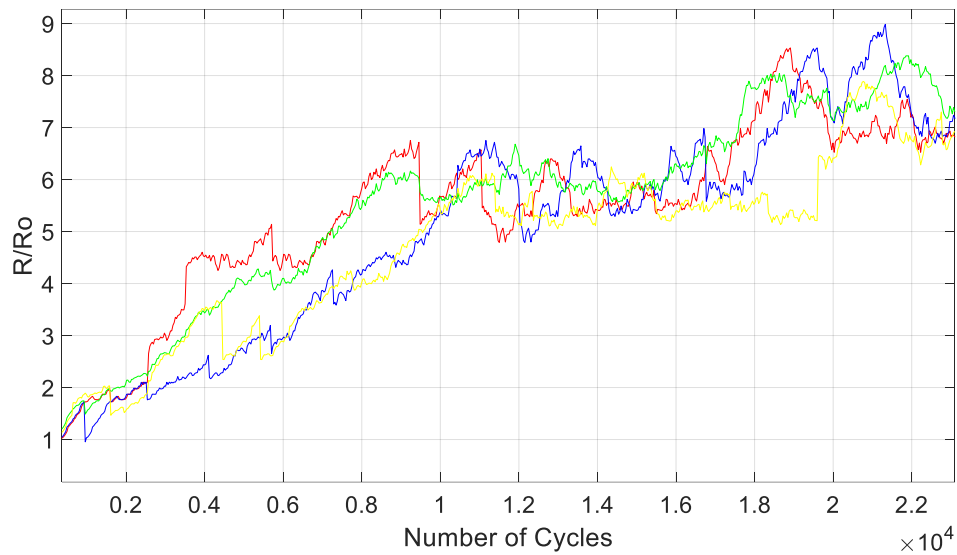


Figure 37 – R/R_0 during fretting wear (four runs) at 10 A

Figure 38 shows the contact resistance ratio during fretting for the four different material combinations at 10 A. The graphs show that average of four runs for each material combination. R/R_0 increases much faster when the ball and the plate are made of the same material than if they are different. R/R_0 exceeds 10 at around 16,000 cycles for similar materials. When the ball and plate are both made of sterling silver, the increase in contact resistance is the highest. As a result for this combination, the experiment is only conducted for about 23,000 cycles as the temperature resulting from the increasing resistance reached around 70°C at the load cell of the tribometer. When the ball and plate are made of dissimilar materials, the increase in contact resistance is slower and R/R_0 is less than 10 after 25,000 cycles. The results show that using electrical contacts made of dissimilar materials result in a reduced increase in contact resistance. This is attributed to the lower chemical affinity of the materials when in contact.

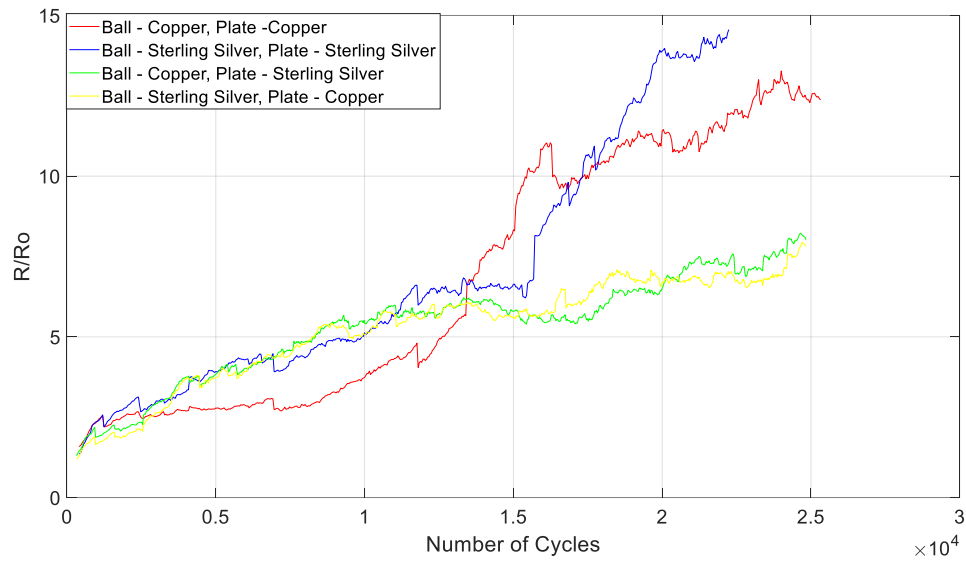


Figure 38 - R/R_0 during fretting wear (four runs) at 10 A for different material combinations

8.3 Thermal Rectification

The extent of thermal rectification between dissimilar contacts is explored using a finite element model and validated experimentally. The validated model is used to predict the improvement in performance of the APA FMS.

8.3.1 Experiment Description

The contact experiment setup in Figure 27 is used to conduct the experiment. spherical contacts with a 10 mm diameter, made of pure copper and aluminium alloy 6061-T6 are attached to the fixed and moving sides of the experiment chamber through copper adaptors, respectively. The copper adaptors are connected to polyether-ether ketone (PEEK) blocks as shown in Fig 39. The temperature is measured at different locations using resistance temperature detectors (RTDs) as current is conducted through the contacts.

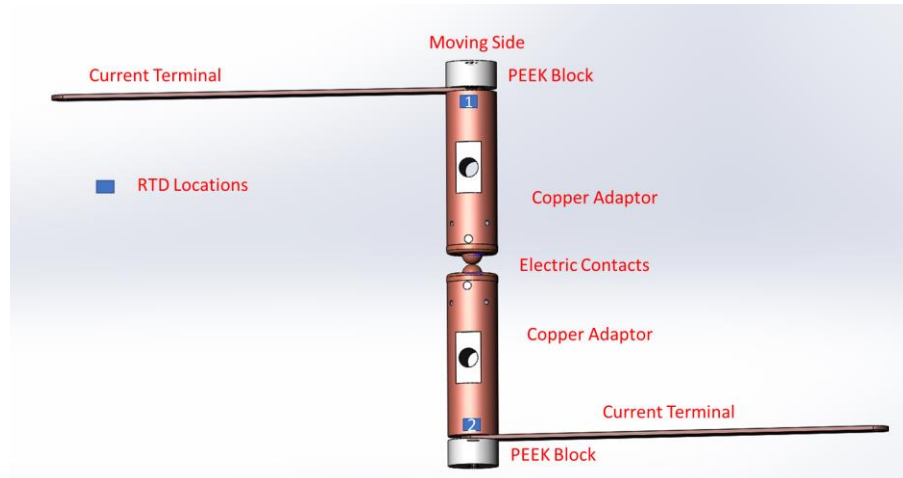


Figure 39 – Thermal Rectification Experiment Components

The RTD sensors used are 3-wire surface mount RTD's which stick to the surface of the metals. The force between the contacts is adjusted by the linear motion actuator on the moving side. The force is measured using a force sensor inserted between the contacts prior to the conduction of current. As a result, the force as a function of the displacement of the linear motion actuator is known and the experiment can be conducted by removing the force sensor. The experiment is conducted Cu-Cu, Al-Al and Cu-Al contact pairs. Most of the heat is generated through Joule heating at the interface of the contact pairs, where the contact resistance is highest. The generated heat flows to the ends of the copper adaptors, which have a lower temperature. As the experiment is not conducted in vacuum, the heat is also dissipated through convection. As a result, the experiments are repeated by swapping the contacts to account for the effect of gravity and the temperature measured by the RTD's are averaged between the two cases, which is expected to minimize the effect of natural convection. The experiments are repeated for each contact combination with a continuous current of 50, 100, 150 and 200 A with a contact force of 25, 50, 100 and 150 N.

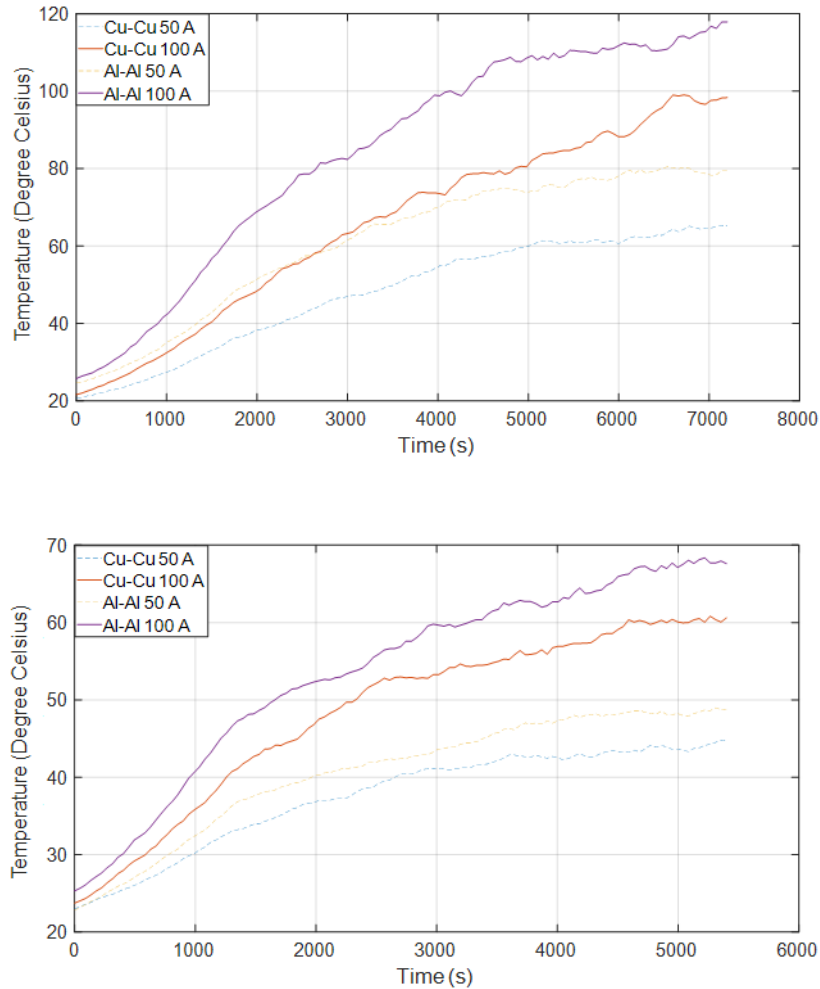


Figure 40 – Temperature on Cu and Al side of copper-copper and aluminum-aluminum contact pairs with a current of 50 A and 100 A and contact force of 25 N (top) and 100 N (bottom).

8.3.2 Experiment Results

Figure 39 shows the locations where the temperature is measured by RTD's. The temperature at RTD locations 1 and 2 are averaged. Figure 40 shows the average temperature vs time curves at 50 and 100 A with a contact force of 25 N and 100 N for Cu-Cu and Al-Al. The results show that contact force, and electrical conductivity as well as

thermal conductivity of the contact materials affect the flow of heat through the contacts. The steady-state temperature is higher for the Al-Al pair as the thermal conductivity and electrical conductivity of aluminium is lower than those of copper. The steady-state temperature is also higher for both Al-Al and Cu-Cu contact pairs when the contact force is lower. The steady-state temperature is reached earlier when the contact force is higher.

Figure 41 shows average temperature versus time curves for Cu-Al contact pairs measured at RTD locations 1 and 2 at 50 A and 100 A with a contact force of 25 N and 100 N. The temperature on the Cu and Al side is measured twice by swapping the contacts and averaged. measured by the RTD's for Al-Cu contact at 50 A and 100 A with a contact force of 100 N. The legend "Copper 100A" in Figure 41 represents the average temperature vs time curve at the end of the copper adaptor on the Cu contact side at 100 A. The legend 'Aluminium 50A' represents the average temperature vs time curve at the end of the copper adaptor on the Al contact side at 100 A.. The results show that the steady-state temperature is lower on the aluminium side than the copper side due to higher electrical and thermal conductivity of copper. Figure 41 a) shows the temperature on the Al side is around 10% lower than the temperature at the Cu-Cu contact pair in Figure 40 a) for both 50 A and 100 A. This shows that the having a Cu-Al contact pair will result in a 10% lower temperature on the Al side independent of the current through the contact pair. Figure 41 b) shows the temperature on the Al side is around 5% lower than the temperature at the Cu-Cu contact pair in Figure 40 b) for both 50 A and 100 A. This shows that the relative reduction of the temperature on the Al side reduces with increasing contact force. To

further extend the study to different current levels, contact forces, and contact materials, a simulation model is developed and compared to the experiment results.

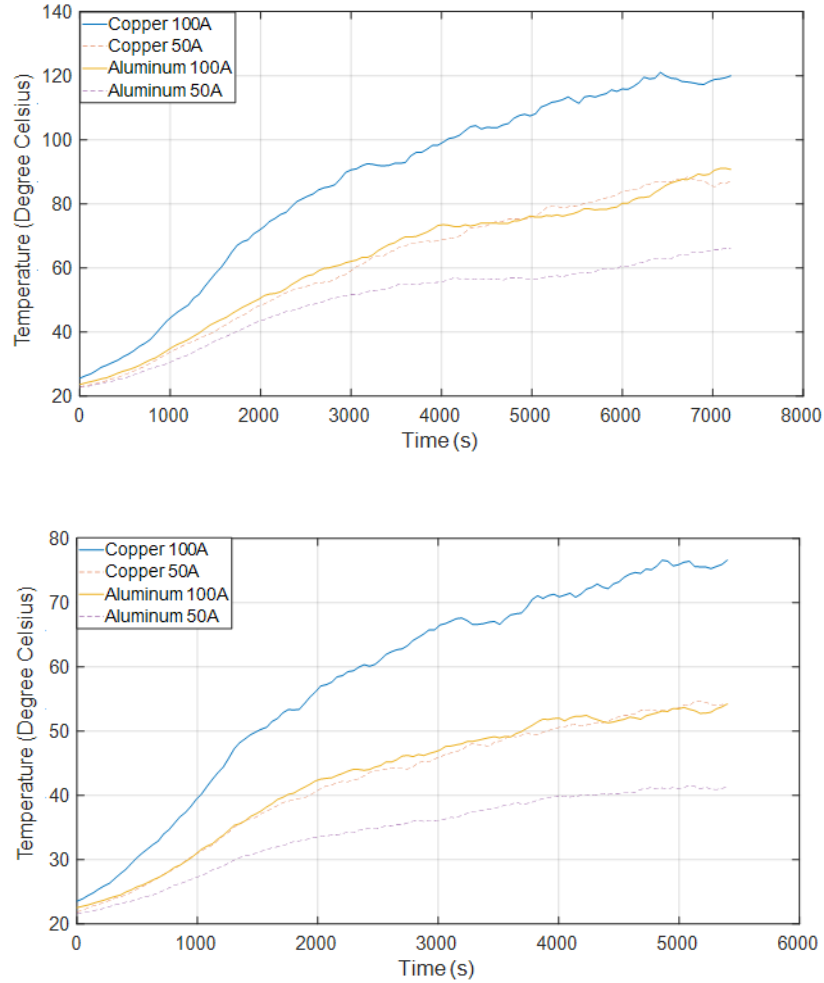


Figure 41 - Temperature on of copper and aluminum side in Cu-Al contact pairs with a current of 50 A and 100 A and contact force of 25 N (top) and 100 N (bottom).

8.3.3 Simulation Model

A finite element simulation model of thermal rectification in similar and dissimilar contact pairs is developed using COMSOL Multiphysics. The multiphysics simulation uses a coupled structural, electrical and thermal model to calculate the temperatures at different

locations of the contacts and copper adaptors as a function electric current and applied force. The set of equations used by COMSOL Multiphysics are:

$$\rho \frac{\partial^2 u}{\partial t^2} = \nabla \cdot (FS)^T + F_v, \quad F = l + \nabla u \quad (35)$$

$$\nabla \cdot J = Q_{j.v}, \quad J = \sigma \cdot E + \frac{\partial D}{\partial t} + J_e, \quad E = -\nabla v \quad (36)$$

$$\rho C_p \cdot \frac{\partial T}{\partial t} + \rho C_p u \cdot \nabla T + \nabla \cdot q = Q + Q_{ted}, \quad q = -k \nabla T \quad (36)$$

Equation (35) deals with the ‘Solid Mechanics’ part of the physics and the equilibrium equations are given by Newton’s second law. The equation is written in Lagrangian form for the material frame formulation, used by COMSOL Multiphysics where S is the second Piola-Kirchhoff stress tensor, F_v is body force per unit deformed volume, ρ is the density of the material and u is the velocity. Equation (36) is used by the Electric Current part of the physics and represents the point form of Ohm’s law in a stationary coordinate system where σ is electrical resistivity, J_e is an externally generated current density, E is the electric field intensity and v is the voltage drop. The Heat Transfer part of the physics is governed by equation (37) which is the set of Energy balance equation and Fourier’s law of conduction. This method has been used in literature for stationary and time domain simulations of sphere-sphere [114] and sphere-plane [115] contacts in COMSOL [116] and ANSYS [117]. The results have been experimentally validated [118].

Figure 42 shows the geometry and boundary conditions of the thermal rectification finite element model. The polymeric insulation block and the braided copper terminals are

not modelled and the boundary conditions for current injection is directly applied to the cross sections of the top and bottom copper adaptors. The mechanical force is applied to the top adaptor and the bottom adaptor is fixed. The mechanical pressure on the contacts can alter the electrical and thermal properties of the material locally around the region surrounding the contacts. Therefore, in order to accurately simulate the current-carrying capability and temperature rise in the switch, it is important to take a more comprehensive approach in the simulation and incorporate the effect of contact pressure to compute the electrical and thermal conductance of the contact surfaces. The boundaries of the two spherical contacts are defined as a contact pair node, which specifies that these boundaries cannot penetrate each other under deformation. Using the ‘Solid Mechanics’ module, the mechanical properties of the contact pair and applied force is specified and the pressure at the interface of the contacts is calculated. The pressure is calculated using the Augmented Lagrangian algorithm [119], which is a standard constrained optimization algorithm used to solve the contact problems in finite element packages [114]. The calculated contact pressure is used as input to the contact pair node in the ‘Electric Current’ module. The electric currents module uses the contact pressure and the electric current boundary conditions to calculate the thermal contact conductance.

The thermal contact conductance is determined using the Cooper-Mikic-Yovanovich (CMY) correlation [120], which is valid for isotropic rough surfaces and has been formulated assuming plastic deformation of the surface asperities. However, this model does not compute nor store the plastic deformation of the asperities. For example, if a load is applied twice, the electrical contact is identical in both cases. The relevant

properties of the surface asperities are average roughness of the upper and lower contacts (σ_u and σ_l) and the average surface slope of the upper and lower contacts (m_u and m_l).

The CMY correlation defines the RMS surface roughness and slope as

$$\sigma = \sqrt{(\sigma_u^2 + \sigma_l^2)}, m = \sqrt{(m_u^2 + m_l^2)} \quad (38)$$

The CMY correlation relates thermal contact conductance h_c to the asperities and pressure load at the contact interface by

$$h_c = 1.24 \sigma_{contact} \frac{m}{\sigma} \left(\frac{p}{H_c} \right)^{0.95} \quad (39)$$

where p is the contact pressure, H is the microhardness of the softer material and $\sigma_{contact}$ is the harmonic mean of the contact surfaces given by

$$\sigma_{contact} = \frac{2\sigma_u\sigma_d}{\sigma_u + \sigma_d} \quad (40)$$

The surface of properties of the Cu and Al samples were measured using an optical profiler. The average roughness of the Cu and Al contacts prior to the experiments were 0.38 μm and 0.53 μm respectively. The average surface slope of the Cu and Al contacts were 0.12 and 0.14, respectively. The microhardness of the Al, which is the softer contact

material, is measured using a Vickers hardness tester, is 65.3 HV. The calculated h_c is used by the 'Heat Transfer' module to obtain the temperature at different points in the geometry.

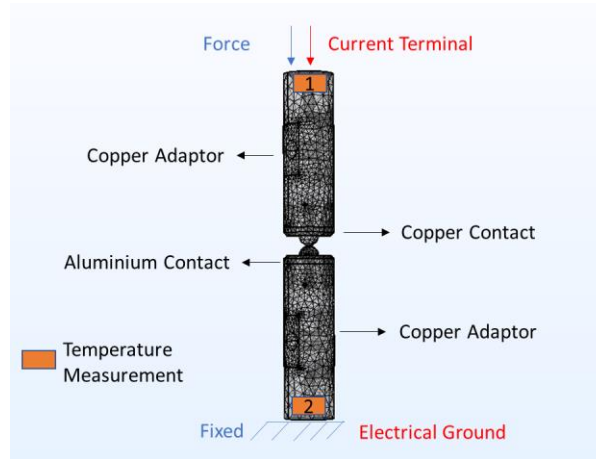


Figure 42 – Simulation model showing boundary conditions and temperature measurement locations.

The exposed surfaces of the model lose heat due to their interaction with air via natural convection. In the simulation, this is modeled by specifying a heat transfer coefficient and the ambient temperature of the surrounding air. Initially, the contact switch is assumed to be at room temperature (20°C). The current flow through the contacts causes a rise in temperature throughout the model, which reaches a steady state value over time. Similar simulation models used to determine temperature rise in automotive components [121], coated spherical contacts [122], as well as rivet contacts [123], and have each been validated by experimental results.

The simulation makes use of a time-dependent solver based on backward Euler method with a maximum of 10000 iterations. The simulation model makes use of free tetrahedral meshes and consists of 76,558 mesh elements with a minimum element quality

of 0.03141. The element sizes are between 0.681 – 9.37 mm with a maximum element growth rate of 1.4 and resolution of narrow regions of 0.7. The simulation model solves for 1.68 million degrees of freedom. A time dependent study with a timestep of 1 minute is takes around 4.5 hours for a given applied current and applied force between the contacts. The simulation model is initially run for Cu-Al contact pairs to validate it against the results from Figure 41. The validated model can then used to determine the extent of thermal rectification for materials pairs that consists of other materials that were not at hand for experimental results such as silver and copper based contact materials.

8.3.4 Results

Figure 43 shows the comparison of the simulation results and the experiment results at 50 A and 100 A at a contact force of 25 N and 100 N at location 1 and 2, respectively. The simulation model shows a close match with the experiment results. The extrapolated steady-state temperature shows a <5% difference between the simulation model and the experiment results for Cu-Cu and Al-Al contacts and <10% difference for Cu-Al contacts. The model is used to extend the study to a range of current levels and contact force. The study can also be extended to different electrical contact materials.

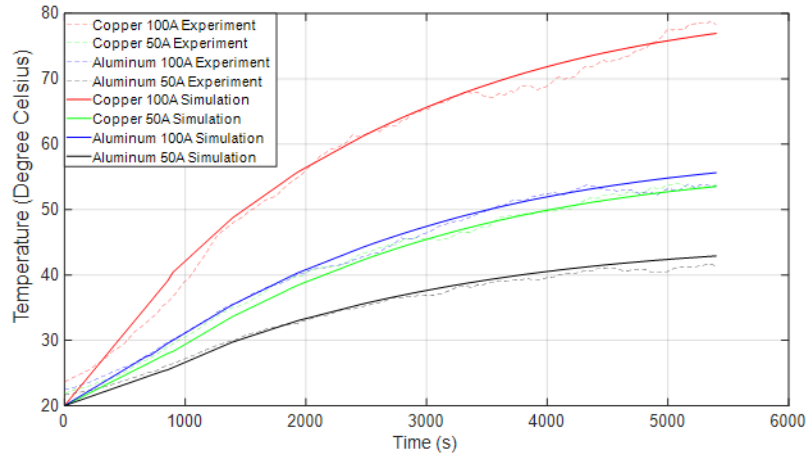
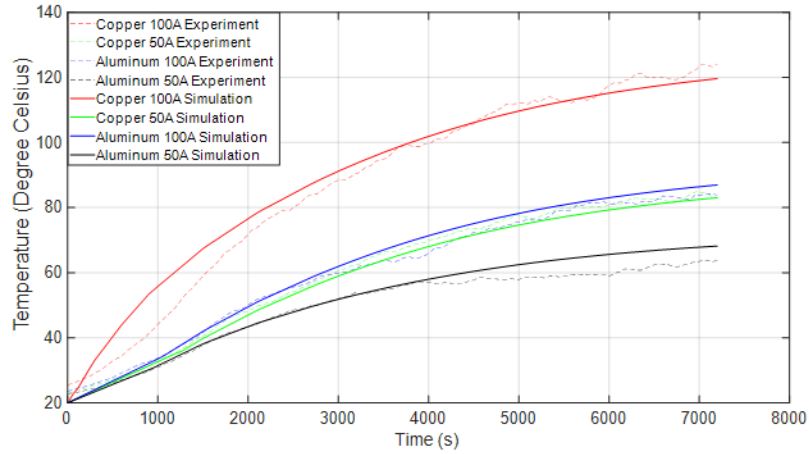


Figure 43 – Comparison of simulation and experimental results for Cu-Al contact pairs with a current of 50 A and 100 A and contact force of 25 N (top) and 100 N (bottom), respectively.

Figure 44 shows the relative reduction in the temperature on the Al side of the Cu-Al pair compared to the temperature of Cu-Cu pair. The temperatures are calculated at RTD locations 1 and 2 in the model. The temperature on the Al side is shown to be around 10% lower and independent of the current. The percentage decrease of temperature on the Al side is around 10.2% at 25 N and reduces to 2.2% as the contact force is increased to 150 N. This shows that the extent of thermal rectification reduces with the increase in

contact force. This translates to around 67.7% of the generated heat flowing through the Cu side of the Cu-Al contacts at 25 N independent of load current. As the applied force is increased, the percentage heat flowing through the Cu side increases slightly to 70.7% at 100 N and 73.1 % at 150 N.

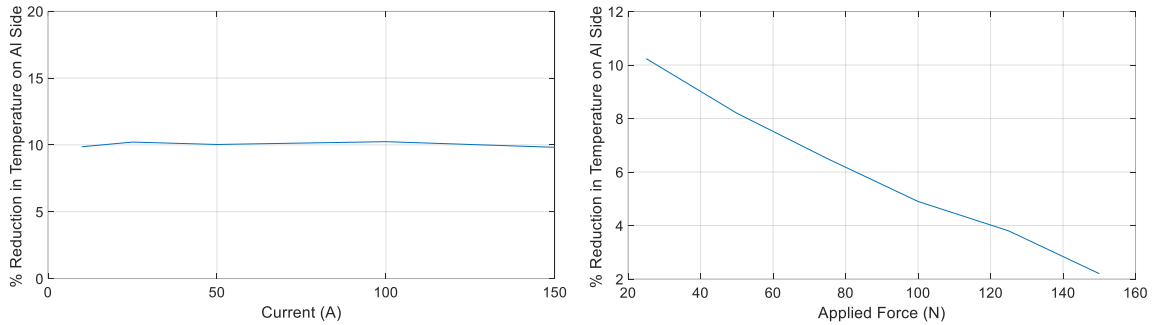


Figure 44 – Relative reduction in temperature on Al side of Al-Cu pair compared to a Cu-Cu pair a) as a function of current at 25 N, b) as a function of applied force at 100 A

Figure 45 shows the relative reduction in temperature as a function of contact force for Cu-Ag contact pair. Silver has a higher electrical (63.0 MS/m vs. 59.4 MS/m) and thermal conductivity (429 W/m.K vs. 385 W/m.K) than copper. As a result, more heat flows through silver contact and the copper side will have the higher temperature. The percentage decrease in temperature of copper is shown to be around 2.9% at a contact force of 25 N independent of load current. The percentage decrease reduces to 0.8% when the contact force increases to 150 N. This translates to around 56.7% of the generated heat flowing through the Ag side of the Cu-Ag contacts at 25 N independent of load current. As the applied force is increased, the percentage heat flowing through the Ag side increases slightly to 57.7% at 100 N and 58.1 % at 150 N.

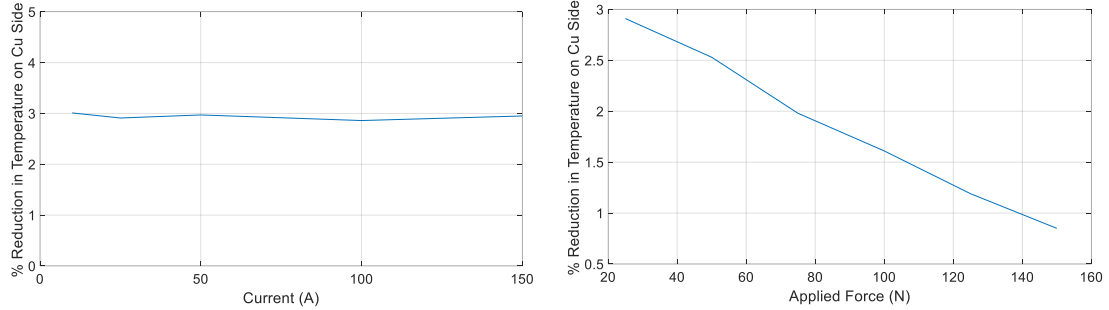


Figure 45 – Relative reduction in temperature on Ag side of Ag-Cu pair compared to a Cu-Cu pair a) as a function of current at 25 N, b) as a function of applied force at 100 A

The results demonstrate that a higher percentage of temperature reduction requires a higher difference in thermal conductivities between the two dissimilar contacts. However, since electrical and thermal conductivities of metals are linearly correlated [124], having dissimilar contact materials made of dissimilar materials may result in a higher contact resistance. This results in higher power loss and higher temperatures at the contact interface. As a result, the selection of the pair of dissimilar materials depends on the trade-off between the power loss limit and temperature limit of the FMS. Materials with high electrical conductivity and low thermal conductivity are preferred for better thermal rectification.

8.4 Summary

The chapter explores two advantages of using dissimilar materials in a contact pair: reduced fretting wear and thermal rectification. The extent of fretting wear is quantified by conducting experiments with similar and dissimilar pairs of copper and sterling silver contacts on the ball-on-flat tribometer. The ratio of contact resistance before and during the experiment (R/R_0) is measured. The R/R_0 is greater than 10 (assumed failure condition)

at around 17,000 cycles of fretting wear for similar contact pairs. The R/R_0 is about 7.5 at around 25,000 cycles for dissimilar contact pairs. No trend is observed for the extent of fretting wear with respect to load current. The results demonstrate the reduced fretting wear using dissimilar contact pairs.

The extent of thermal rectification is explored using similar and dissimilar pairs of copper and aluminium contacts using the contact experiment setup. The results show a 10% reduction in the temperature on the aluminium side at 25 N of applied force and 100 A of applied current. A finite element model developed based on thermal contact conductance between the contact pairs determined by the CMY correlation is validated by the experiment results. The validated model is used to extend the study to different current levels, applied force and contact material pairs. The model shows that the relative thermal rectification is independent of load current and reduces as the applied force increases. The extent of thermal rectification is found to be greater when the difference in thermal conductivities of the two contact materials is higher. This results in a trade-off between the power loss and the temperature limit of the FMS.

CHAPTER 9. CONCLUSION

This dissertation explored the design considerations for electrical contacts for Fast Mechanical Switches (FMS) for use in hybrid circuit breakers. The design considerations were explored for two piezoelectric FMS prototypes for medium voltage applications capable of opening in less than a millisecond. One of the prototypes is based on an amplified piezoelectric actuator (APA) and the other on a linear piezoelectric actuator. The design of electrical contacts are crucial to the performance of both these piezoelectric FMS. The research conducted demonstrates the constraints on the mass and geometry of the contacts from using piezoelectric actuators through finite element and spring mass simulations. The results show that APAs with higher aspect ratios not only have larger stroke but they also have higher contact bounce and the contacts take longer to reach their steady state separation distance for a given length of piezoelectric stack. The mass of the contacts was also found to affect the travel curve with lighter contacts separating faster and with lower bounce. The overshoot in the travel curve increases with contact mass, which makes the FMS susceptible to restrike by transient recovery voltage.

The most suitable electrical contact materials were identified through the Ashby method. The materials were ranked based on the relative importance of the performance indices. The results show that aluminum, silver and copper-based materials are the best materials if minimizing wear has high priority. Copper, aluminum and copper-based materials are the best materials if minimizing wear and overheating have equal priority. Copper-based materials are the best materials if minimizing overheating (and power loss)

has a relatively higher priority. The results show that copper-based materials rank highly in all the cases shown and are more suitable for FMS contacts compared to silver-based materials and any other material considered.

The research also explored electrical contact geometries to minimize the electric field when open. Optimized contact geometries with uniform field profiles such as (and Rogowski and Bruce) were found to have lower peak electric field than spherical and flat contacts. These contacts also have enough surface area that their contact resistance is lower than spherical and elliptical contacts. The impact of fretting wear on the voltage rating of FMS was studied by conducting fretting experiments on a tribometer and measuring the surface properties of the contacts afterwards. The breakdown voltage after fretting was estimated using finite element models and streamer breakdown criterion. Fretting wear was shown to alter the surface structure of the contacts, which results in lower breakdown voltage.

The research also explored using dissimilar materials in a contact pair to improve the performance of FMS. Fretting experiments using Sterling silver and copper contacts show that the rise of contact resistance with fretting wear of dissimilar materials compared to fretting wear of similar materials. Thermal rectification experiments and simulation models show that the extent of rectification is independent of the load current and inversely proportional to the contact force. Thermal rectification is also greater when the difference in thermal conductivities of the dissimilar materials are greater. The selection of the optimal materials depends on the trade-off between the allowable power loss of the FMS and the

temperature limits of the various components of the FMS. impact on the voltage and current rating of the FMS.

CHAPTER 10. FUTURE WORK

The design constraints for electrical contacts of FMS were first obtained from static and spring mass simulations. The physics of the piezoelectric actuator stack is not modelled in this paper and including it in the model can lead to more accurate results. The determination of limits on contact mass due to a trade-off between the current and voltage rating of the FMS can be explored in more detail by considering the geometry and dissimilar materials from Chapter 6 and Chapter 8.

The most suitable contact materials obtained from the Ashby method can be verified by conducting experiments on the top ranked candidate materials. Also, the analysis assumed that the pair of contacts are made of the same materials. The Ashby method can be expanded to select the best performing pair of dissimilar contact materials. Also, contact can be made of layers of different materials that have different desirable properties. These graded contacts can lead to better performance than contacts made of the same materials and can be explored by the Ashby method.

Further research needs to be done on the effect of surface roughness on the contact resistance. The long-term performance of contacts with optimized geometries also needs to be investigated. The fretting experiments can be conducted for high ranked materials with higher hardness than copper, to determine the roughness parameters as a function of load current. As the FMS is typically rated for > 600 A, the voltage derating due to fretting wear could be potentially greater at higher currents and needs to be studied further. The

voltage derating can also be experimentally validated with high voltage breakdown experiments.

The thermal rectification model can be further improved by developing a thermal network model which helps better understand the interaction between different components and types of heat transfer in the thermal rectification experiment. The experiments can be expanded to study metal matrix composites and 3D printed metals to verify if the results from the simulation model hold up for these materials. The extent of thermal rectification can be evaluated on the geometry of a real FMS prototype. This informs the dependence on the utility of thermal rectification on the trade-off between the allowable power loss of the FMS and the temperature limits of the various components of the FMS.

REFERENCES

- [1] W. Breuer, D. Povh, D. Retzmann, and E. Teltsch, "Trends for future HVDC Applications," *16th CEPSI, November*, pp. 6-10, 2006.
- [2] N. Doerry and J. Amy, "The road to MVDC," in *ASNE Intelligent Ships Symposium*, 2015, pp. 20-21.
- [3] R. Alexander, D. Meyer, and J. Wang, "A comparison of electric vehicle power systems to predict architectures, voltage levels, power requirements, and load characteristics of the future all-electric aircraft," in *2018 IEEE Transportation Electrification Conference and Expo (ITEC)*, 2018: IEEE, pp. 194-200.
- [4] A. T. Elsayed, A. A. Mohamed, and O. A. Mohammed, "DC microgrids and distribution systems: An overview," *Electric power systems research*, vol. 119, pp. 407-417, 2015.
- [5] G. F. Reed, B. M. Grainger, A. R. Sparacino, R. J. Kerestes, and M. J. Korytowski, "Advancements in medium voltage DC architecture development with applications for powering electric vehicle charging stations," in *2012 IEEE Energytech*, 2012: IEEE, pp. 1-8.
- [6] M. Stieneker and R. W. De Doncker, "Medium-voltage DC distribution grids in urban areas," in *2016 IEEE 7th International Symposium on Power Electronics for Distributed Generation Systems (PEDG)*, 2016: IEEE, pp. 1-7.
- [7] X. Li, Z. Yuan, J. Fu, Y. Wang, T. Liu, and Z. Zhu, "Nanao multi-terminal VSC-HVDC project for integrating large-scale wind generation," in *2014 IEEE PES General Meeting/ Conference & Exposition*, 2014: IEEE, pp. 1-5.
- [8] Z. Jie *et al.*, "Research of DC circuit breaker applied on Zhoushan multi-terminal VSC-HVDC project," in *2016 IEEE PES Asia-Pacific Power and Energy Engineering Conference (APPEEC)*, 2016: IEEE, pp. 1636-1640.
- [9] A. Giannakis and D. Pefitsis, "Mvdc distribution grids and potential applications: Future trends and protection challenges," in *2018 20th European Conference on Power Electronics and Applications (EPE'18 ECCE Europe)*, 2018: IEEE, pp. P. 1-P. 9.
- [10] Y. Khersonsky *et al.*, "Recommended Practice for 1 to 35 kV Medium Voltage DC Power Systems on Ships," 2010.
- [11] "IEEE Standard for AC High-Voltage Circuit Breakers Rated on a Symmetrical Current Basis - Preferred Ratings and Related Required Capabilities for Voltages Above 1000 V," *IEEE Std C37.06-2009*, pp. 1-46, 2009, doi: 10.1109/IEEESTD.2009.5318709.
- [12] A. Hassanpoor, J. Häfner, and B. Jacobson, "Technical assessment of load commutation switch in hybrid HVDC breaker," *IEEE Transactions on power electronics*, vol. 30, no. 10, pp. 5393-5400, 2014.
- [13] M. M. Walter, "Switching arcs in passive resonance HVDC circuit breakers," ETH Zurich, 2013.

- [14] Y. Wu, Y. Hu, Y. Wu, M. Rong, and Q. Yi, "Investigation of an active current injection dc circuit breaker based on a magnetic induction current commutation module," *IEEE Transactions on Power Delivery*, vol. 33, no. 4, pp. 1809-1817, 2018.
- [15] V. Lenz, "DC current breaking solutions in HVDC applications," ETH Zürich, 2015.
- [16] J.-M. Meyer and A. Rufer, "A DC hybrid circuit breaker with ultra-fast contact opening and integrated gate-commutated thyristors (IGCTs)," *IEEE Transactions on Power Delivery*, vol. 21, no. 2, pp. 646-651, 2006.
- [17] J. Häfner and B. Jacobson, "Device and method to break the current of a power transmission or distribution line and current limiting arrangement," ed: Google Patents, 2014.
- [18] M. Noe and M. Steurer, "High-temperature superconductor fault current limiters: concepts, applications, and development status," *Superconductor science and technology*, vol. 20, no. 3, p. R15, 2007.
- [19] C. Meyer, M. Kowal, and R. W. De Doncker, "Circuit breaker concepts for future high-power DC-applications," in *Industry Applications Conference, 2005. Fourtieth IAS Annual Meeting. Conference Record of the 2005*, 2005, vol. 2: IEEE, pp. 860-866.
- [20] P. Skarby, "High voltage DC breaker apparatus," ed: Google Patents, 2015.
- [21] T. Eriksson, M. Backman, and S. Halén, "A low loss mechanical HVDC breaker for HVDC Grid applications," *Proc. Cigré Session, Paris, France*, 2014.
- [22] D. Andersson and A. Henriksson, "Passive and active DC breakers in the three Gorges-Changzhou HVDC project," in *Proceedings of the International Conference on Power Systems. Wuhan, China: CIGRE*, 2001, pp. 391-395.
- [23] E. Gaxiola and J. Vogelsang, "DC voltage circuit breaker," ed: Google Patents, 2016.
- [24] S. Yanabu, T. Tamagawa, S. Irokawa, T. Horiuchi, and S. Tomimuro, "Development of HVDC circuit breaker and its interrupting test," *IEEE Transactions on Power Apparatus and Systems*, no. 7, pp. 1958-1965, 1982.
- [25] Z. Shi, Y. Zhang, S. Jia, X. Song, L. Wang, and M. Chen, "Design and numerical investigation of a HVDC vacuum switch based on artificial current zero," *IEEE Transactions on Dielectrics and Electrical Insulation*, vol. 22, no. 1, pp. 135-141, 2015.
- [26] B.-C. Kim, Y.-H. Chung, H.-D. Hwang, and H.-S. Mok, "Development of HVDC circuit breaker with fast interruption speed," in *Power Electronics and ECCE Asia (ICPE-ECCE Asia), 2015 9th International Conference on*, 2015: IEEE, pp. 2844-2848.
- [27] *IEEE Guide for Fault Current Limiter (FCL) Testing of FCLs Rated above 1000 V AC*, IEEE, IEEE Std C37.302-2015, 18 May 2016 2016. [Online]. Available: <http://ieeexplore.ieee.org/stamp/stamp.jsp?tp=&arnumber=7473798&isnumber=7473797>

- [28] T. G. Alvin, I. Z. Abidin, and H. Hashim, "Changes in fault current levels due to renewable embedded generation in a distribution network," in *Clean Energy and Technology (CEAT), 2013 IEEE Conference on*, 2013: IEEE, pp. 254-258.
- [29] T. M. Masaud and R. D. Mistry, "Fault current contribution of Renewable Distributed Generation: An overview and key issues," in *Technologies for Sustainability (SusTech), 2016 IEEE Conference on*, 2016: IEEE, pp. 229-234.
- [30] X. Pei, O. Cwikowski, D. Vilchis-Rodriguez, M. Barnes, A. Smith, and R. Shuttleworth, "A review of technologies for MVDC circuit breakers," in *Industrial Electronics Society, IECON 2016-42nd Annual Conference of the IEEE*, 2016: IEEE, pp. 3799-3805.
- [31] A. Challita and M. Uva, "High speed medium voltage direct current isolation device," in *Proc. ASNE Electr. Mach. Technol. Symp.(EMTS)*, 2014, pp. 248-257.
- [32] C. Peng, I. Husain, A. Q. Huang, B. Lequesne, and R. Briggs, "A Fast Mechanical Switch for Medium-Voltage Hybrid DC and AC Circuit Breakers," *IEEE Transactions on Industry Applications*, vol. 52, no. 4, pp. 2911-2918, 2016, doi: 10.1109/tia.2016.2539122.
- [33] L. Graber, S. Smith, D. Soto, I. Nowak, J. Owens, and M. Steurer, "A new class of high speed disconnect switch based on piezoelectric actuators," in *Electric Ship Technologies Symposium (ESTS), 2015 IEEE*, 2015: IEEE, pp. 312-317.
- [34] K. Yasuoka, K. Nakayama, S. Kubo, and S. Zen, "Arcless Current Interruption of DC 150A using a Hybrid DC Circuit Breaker Consisting of SiC-MOSFET and Metal Contacts."
- [35] D. Vilchis-Rodriguez, R. Shuttleworth, and M. Barnes, "Double-sided Thomson coil based actuator: Finite element design and performance analysis," 2016.
- [36] A. Bissal, J. Magnusson, and G. Engdahl, "Comparison of two ultra-fast actuator concepts," *IEEE Transactions on Magnetics*, vol. 48, no. 11, pp. 3315-3318, 2012.
- [37] B. Roodenburg, M. A. Kaanders, and T. Huijser, "First results from an electromagnetic (EM) drive high acceleration of a circuit breaker contact for a hybrid switch," in *Power Electronics and Applications, 2005 European Conference on*, 2005: IEEE, pp. 10 pp.-P. 10.
- [38] X. Xiaodong, L. Zhibing, Y. Xianlgian, L. Beiyang, and T. Yang, "Design and test of vacuum circuit breaker with hybrid fast operating mechanism," in *Electric Power Equipment-Switching Technology (ICEPE-ST), 2017 4th International Conference on*, 2017: IEEE, pp. 939-946.
- [39] W. Wen *et al.*, "Research on operating mechanism for ultra-fast 40.5-kV vacuum switches," *IEEE Transactions on Power Delivery*, vol. 30, no. 6, pp. 2553-2560, 2015.
- [40] P. Skarby and U. Steiger, "An ultra-fast disconnecting switch for a hybrid HVDC breaker—A technical breakthrough," in *CIGRE Canada Conference*, 2013.
- [41] B. Roodenburg and B. H. Evenblij, "Design of a fast linear drive for (hybrid) circuit breakers—Development and validation of a multi domain simulation environment," *Mechatronics*, vol. 18, no. 3, pp. 159-171, 2008.
- [42] C. Peng, I. Husain, and A. Q. Huang, "Evaluation of design variables in Thomson coil based operating mechanisms for ultra-fast opening in hybrid AC and DC circuit

- breakers," in *Applied Power Electronics Conference and Exposition (APEC), 2015 IEEE*, 2015: IEEE, pp. 2325-2332.
- [43] K. Uchino, "Introduction to piezoelectric actuators and transducers," PENNSYLVANIA STATE UNIV UNIVERSITY PARK, 2003.
- [44] P. A. York, N. T. Jafferis, and R. J. Wood, "Meso scale flextensional piezoelectric actuators," *Smart Materials and Structures*, vol. 27, no. 1, p. 015008, 2017.
- [45] T. Yano, S. K. Chee, K. Yakuwa, S. Harada, and T. Higuchi, "A new type of mechanical transformer with high stroke magnification ratio," *Simulation*, vol. 10, no. 1600, p. 18, 2008.
- [46] L. Graber, C. Widener, S. Smith, and M. Steurer, "Ultrafast electromechanical disconnect switch," Patent Appl. US20160329182A1, 2016.
- [47] M. Bosworth, D. Soto, R. Agarwal, M. Steurer, T. Damle, and L. Graber, "High speed disconnect switch with piezoelectric actuator for medium voltage direct current grids," in *2017 IEEE Electric Ship Technologies Symposium (ESTS)*, 14-17 Aug. 2017 2017, pp. 419-423, doi: 10.1109/ESTS.2017.8069316.
- [48] C. Xu *et al.*, "Piezoelectrically Actuated Fast Mechanical Switch for MVDC Protection," *IEEE Transactions on Power Delivery*, 2020.
- [49] S. Zen, T. Hayakawa, K. Nakayama, and K. Yasuoka, "Development of an arcless DC circuit break using a mechanical contact and a semiconductor device," in *Electrical Contacts, 2017 IEEE Holm Conference on*, 2017: IEEE, pp. 249-252.
- [50] T. D. Chunmeng Xu, Lukas Graber, "A Survey on Mechanical Switches for Hybrid Circuit Breakers," presented at the IEEE Power and Energy Society General Meeting Atlanta, GA USA, 2019.
- [51] L. Graber, C. Widener, S. Smith, and M. Steurer, "Ultrafast electromechanical disconnect switch," ed: Google Patents, 2016.
- [52] L. Graber, C. Widener, S. Smith, and M. Steurer, "Thermal-Electrical Study of an Ultra-fast Disconnect Switch with a Piezoelectric Actuator," in *COMSOL Conference*, 2014.
- [53] M. Bosworth, D. Soto, R. Agarwal, M. Steurer, T. Damle, and L. Graber, "High speed disconnect switch with piezoelectric actuator for medium voltage direct current grids," in *Electric Ship Technologies Symposium (ESTS), 2017 IEEE*, 2017: IEEE, pp. 419-423.
- [54] J. Wei, A. Cruz, C. Xu, F. Haque, C. Park, and L. Graber, "A Review on Dielectric Properties of Supercritical Fluids," in *2020 IEEE Electrical Insulation Conference (EIC)*, 2020: IEEE, pp. 107-113.
- [55] Z. Jin, "Efficient DC Interrupter with Surge Protection (EDISON) Q4 2020 Report," in "Efficient DC Interrupter with Surge Protection (EDISON) " Georgia Institute of Technology, 2020.
- [56] J. Ambier and P. Perdigon, "Fretting corrosion of separable electrical contacts," *IEEE transactions on components, hybrids, and manufacturing technology*, vol. 8, no. 1, pp. 197-201, 1985.
- [57] M. Filippakou, C. Karagiannopoulos, D. Agoris, and P. Bourkas, "Electrical contact overheating under short-circuit currents," *Electric Power Systems Research*, vol. 57, no. 2, pp. 141-147, 2001.

- [58] V. Behrens, T. Honig, A. Kraus, E. Mahle, R. Michal, and K. Saeger, "Test results of different silver/graphite contact materials in regard to applications in circuit breakers," in *Electrical Contacts, 1995., Proceedings of the Forty-First IEEE Holm Conference on*, 1995: IEEE, pp. 393-397.
- [59] F. Heitzinger, H. Kippenberg, K. Saeger, and K.-H. Schroder, "Contact materials for vacuum switching devices," *IEEE transactions on plasma science*, vol. 21, no. 5, pp. 447-453, 1993.
- [60] F. Findik and H. Uzun, "Microstructure, hardness and electrical properties of silver-based refractory contact materials," *Materials & design*, vol. 24, no. 7, pp. 489-492, 2003.
- [61] M. Lindmayer and M. Roth, "Contact resistance and arc erosion of W/Ag and WC/Ag," *IEEE Transactions on Components, Hybrids, and Manufacturing Technology*, vol. 2, no. 1, pp. 70-75, 1979.
- [62] M. F. Ashby and D. Cebon, "Materials selection in mechanical design," *Le Journal de Physique IV*, vol. 3, no. C7, pp. C7-1-C7-9, 1993.
- [63] N. G. Trinh, "Electrode design for testing in uniform field gaps," *IEEE Transactions on Power Apparatus and Systems*, no. 3, pp. 1235-1242, 1980.
- [64] W. Rogowski, "Die elektrische festigkeit am rande des plattenkondensators," *Archiv für Elektrotechnik*, vol. 12, no. 1, pp. 1-15, 1923.
- [65] G. C. Lim, T. Damle, and L. Graber, "Optimized contact geometries for high speed disconnect switches," in *Electrical Insulation and Dielectric Phenomenon (CEIDP), 2017 IEEE Conference on*, 2017: IEEE, pp. 537-542.
- [66] F. Bruce, "Calibration of uniform-field spark-gaps for high-voltage measurement at power frequencies," *Journal of the Institution of Electrical Engineers-Part II: Power Engineering*, vol. 94, no. 38, pp. 138-149, 1947.
- [67] S. Anufrik, A. Volodenkov, and K. Znosko, "Selection of electrodes profile for excimer lasers," in *Laser and Fiber-Optical Networks Modeling (LFNM), 2010 10th International Conference on*, 2010: IEEE, pp. 198-200.
- [68] I. Leyva and J. Guerra, "A compacted Ernst-electrodes profile for pulsed high-pressure lasers," *Measurement Science and Technology*, vol. 10, pp. N1-N2, 1999.
- [69] T. Chang, "Improved Uniform-Field Electrode Profiles for TEA Laser and High-Voltage Applications," *Review of Scientific Instruments*, vol. 44, no. 4, pp. 405-407, 1973.
- [70] T. Damle and L. Graber, "Theoretical and Experimental Work on Optimal Contact Geometries on Fast Mechanical Disconnect Switches," in *2018 IEEE Holm Conference on Electrical Contacts*, 2018: IEEE, pp. 24-30.
- [71] S. Fouvry *et al.*, "Fretting wear of low current electrical contacts: Quantification of electrical endurance," in *2017 IEEE Holm Conference on Electrical Contacts*, 2017: IEEE, pp. 1-11.
- [72] R. G. Horn and D. T. Smith, "Contact electrification and adhesion between dissimilar materials," *Science*, vol. 256, no. 5055, pp. 362-364, 1992.
- [73] C. B. Gwyn Jr, "Dissimilar compositions for electrical contact pairs," ed: Google Patents, 1970.

- [74] P. Stevenson, G. Peterson, and L. Fletcher, "Thermal rectification in similar and dissimilar metal contacts," *Journal of Heat Transfer*, vol. 113, no. 1, pp. 30-36, 1991.
- [75] M. Sikorski, "The adhesion of metals and factors that influence it," *Wear*, vol. 7, no. 2, pp. 144-162, 1964.
- [76] "Piezoelectric Actuators Product and Warranty Information." Cedrat Technologies. <http://www.cedrat-technologies.com> (accessed May, 2020).
- [77] R. D. D'Souza, B. Benny, A. Sequeira, and N. Karanth, "Hysteresis modeling of amplified piezoelectric stack actuator for the control of the microgripper," *American Scientific Research Journal for Engineering, Technology, and Sciences (ASRJETS)*, vol. 15, no. 1, pp. 265-281, 2016.
- [78] S. Karunanidhi and M. Singaperumal, "Mathematical modelling and experimental characterization of a high dynamic servo valve integrated with piezoelectric actuator," *Proceedings of the Institution of Mechanical Engineers, Part I: Journal of Systems and Control Engineering*, vol. 224, no. 4, pp. 419-435, 2010.
- [79] Y. Song *et al.*, "Reducing the Fault-Transient Magnitudes in Multiterminal HVdc Grids by Sequential Tripping of Hybrid Circuit Breaker Modules," *IEEE Transactions on Industrial Electronics*, vol. 66, no. 9, pp. 7290-7299, 2018.
- [80] G. C. Lim, T. Damle, and L. Graber, "Optimized contact geometries for high speed disconnect switches," in *2017 IEEE Conference on Electrical Insulation and Dielectric Phenomenon (CEIDP)*, 2017: IEEE, pp. 537-542.
- [81] Y. Kurita, F. Sugihara, J. Ueda, and T. Ogasawara, "Piezoelectric tweezer-type end effector with force-and displacement-sensing capability," *IEEE/ASME Transactions on Mechatronics*, vol. 17, no. 6, pp. 1039-1048, 2011.
- [82] J. Schultz and J. Ueda, "Two-port network models for compliant rhomboidal strain amplifiers," *IEEE Transactions on Robotics*, vol. 29, no. 1, pp. 42-54, 2012.
- [83] T. Damle, M. Varenberg, and L. Graber, "Electric Contact Material Selection for Medium and High Voltage DC Circuit Breakers," *Transactions on Electrical and Electronic Materials*, pp. 1-10, 2020.
- [84] N. Brifcani, R. Day, D. Walker, S. Hughes, K. Ball, and D. Price, "A review of cutting-edge techniques for material selection," in *2nd international conference on advanced composite materials and technologies for aerospace applications*, 2012, pp. 58-64.
- [85] R. A. Aliev, J. Kacprzyk, W. Pedrycz, M. Jamshidi, and F. M. Sadikoglu, *13th International Conference on Theory and Application of Fuzzy Systems and Soft Computing—ICAFS-2018*. Springer, 2018.
- [86] S. Opricovic, "Programski paket VIKOR za visekriterijumsko kompromisno rangiranje," in *17th International symposium on operational research SYM-OP-IS*, 1990.
- [87] G.-H. Tzeng and J.-J. Huang, *Multiple attribute decision making: methods and applications*. CRC press, 2011.
- [88] C. EduPack, "Granta Design Ltd," *Cambridge UK (www.grantadesign.com/education)*, 2016.
- [89] V. Pareto, *Manuale di economia politica*. Societa Editrice, 1906.

- [90] S. Opricovic and G.-H. Tzeng, "Compromise solution by MCDM methods: A comparative analysis of VIKOR and TOPSIS," *European journal of operational research*, vol. 156, no. 2, pp. 445-455, 2004.
- [91] M. Buggy and C. Conlon, "Material selection in the design of electrical connectors," *Journal of materials processing technology*, vol. 153, pp. 213-218, 2004.
- [92] P. Frey, N. Klink, R. Michal, and K. E. Saeger, "Metallurgical aspects of contact materials for vacuum switching devices," *IEEE Transactions on Plasma Science*, vol. 17, no. 5, pp. 734-740, 1989.
- [93] B. G. Watkins, "Materials selection and evaluation of Cu-W particulate composites for extreme electrical contacts," Georgia Institute of Technology, 2011.
- [94] D. Amft, "Selection of the contact material for low-voltage contactors," in *Proceedings of 17th International Symposium on Discharges and Electrical Insulation in Vacuum*, 1996, vol. 2: IEEE, pp. 732-736.
- [95] R. A. Coutu Jr, P. E. Kladitis, K. D. Leedy, and R. L. Crane, "Selecting metal alloy electric contact materials for MEMS switches," *Journal of Micromechanics and Microengineering*, vol. 14, no. 8, p. 1157, 2004.
- [96] V. B. Sawant, S. S. Mohite, and L. N. Cheulkar, "Comprehensive contact material selection approach for RF MEMS switch," *Materials Today: Proceedings*, vol. 5, no. 4, pp. 10704-10711, 2018.
- [97] D. Deshmukh and M. Angira, "Investigation on Switching Structure Material Selection for RF-MEMS Shunt Capacitive Switches Using Ashby, TOPSIS and VIKOR," *Transactions on Electrical and Electronic Materials*, vol. 20, no. 3, pp. 181-188, 2019.
- [98] L. G. Tushar Damle, "Theoretical and Experimental Work on Optimal Contact Geometries for Fast Mechanical Disconnect Switches," in *IEEE Holm Conference on Electrical Contacts*, Albuquerque, NM, USA, 2018, vol. 64, 2018, pp. 24-30.
- [99] M. Varenberg, "Towards a unified classification of wear," *Friction*, vol. 1, no. 4, pp. 333-340, 2013.
- [100] M. Braunovic, "Fretting in electrical/electronic connections: a review," *IEICE transactions on electronics*, vol. 92, no. 8, pp. 982-991, 2009.
- [101] A. Lee, A. Mao, and M. Mamrick, "Fretting corrosion of tin at elevated temperatures," in *Electrical Contacts, 1988., Proceedings of the Thirty Fourth Meeting of the IEEE Holm Conference on Electrical Contacts*, 1988: IEEE, pp. 87-91.
- [102] M. Braunovic, "Effect of contact load on the contact resistance behaviour of different conductor and contact materials under fretting conditions," *Proc. 19th ICEC, Nuremberg, 1998*, pp. 283-287, 1998.
- [103] M. Varenberg, I. Etsion, and G. Halperin, "Slip index: a new unified approach to fretting," (in English), *Tribol. Lett.*, vol. 17, no. 3, pp. 569-573, Oct 2004, doi: 10.1023/B:Tril.0000044506.98760.F9.
- [104] E. Vinaricky, G. Horn, and V. Behrens, "Doduco Data Book of Electrical Contact," *New Edition, Pforzheim: Doduco GmbH, (Pub. Stieglitz Verlag, Muehlacker, Germany)*, 2010.

- [105] Y. W. Park, G. R. Bapu, and K. Y. Lee, "The influence of current load on fretting of electrical contacts," *Tribology International*, vol. 42, no. 5, pp. 682-689, 2009.
- [106] W. Ren, P. Wang, J. Song, and G. Zhai, "Effects of current load on wear and fretting corrosion of gold-plated electrical contacts," *Tribology International*, vol. 70, pp. 75-82, 2014.
- [107] Y. Zeroukhi, E. Napieralska-Juszczak, G. Vega, K. Komez, F. Morganti, and S. Wiak, "Dependence of the Contact Resistance on the Design of Stranded Conductors," *Sensors*, vol. 14, no. 8, pp. 13925-13942, 2014.
- [108] M. Varenberg, G. Halperin, and I. Etsion, "Different aspects of the role of wear debris in fretting wear," *Wear*, vol. 252, no. 11-12, pp. 902-910, 2002.
- [109] G. T. Flowers, F. Xie, M. J. Bozack, and R. D. Malucci, "Vibration thresholds for fretting corrosion in electrical connectors," *IEEE Transactions on Components and Packaging Technologies*, vol. 27, no. 1, pp. 65-71, 2004.
- [110] B. Sjodin, "How to Generate Random Surfaces in COMSOL Multiphysics®| COMSOL Blog," ed.
- [111] O. C. Feet, F. Mauseth, and K. Niayesh, "Influence of Surface Roughness on Breakdown in Air Gaps at Atmospheric Pressure Under Lightning Impulse," in *2018 IEEE International Conference on High Voltage Engineering and Application (ICHVE)*, 2018: IEEE, pp. 1-4.
- [112] W. Zaengl and K. Petcharak, "Application of Streamer Breakdown Criterion for Inhomogeneous Fields in Dry Air and SF 6," in *Gaseous Dielectrics VII*: Springer, 1994, pp. 153-159.
- [113] H. Kwon *et al.*, "Investigation of similar and dissimilar metal contacts for reliable radio frequency microelectromechanical switches," *Japanese Journal of Applied Physics*, vol. 47, no. 8R, p. 6558, 2008.
- [114] F. Pennec, H. Achkar, D. Peyrou, R. Plana, P. Pons, and F. Courtade, "Verification of contact modeling with COMSOL multiphysics software," 2007.
- [115] N. Pandey, I. Jain, S. Reddy, and N. P. Gulhane, "Electro-thermal analysis of contact resistance," in *AIP Conference Proceedings*, 2018, vol. 1966, no. 1: AIP Publishing LLC, p. 020017.
- [116] A. Foley, "Analyzing Electrical and Thermal Conductance in a Contact Switch."
- [117] A. Monnier, B. Froidurot, C. Jarrige, R. Meyer, and P. Testé, "A mechanical, electrical, thermal coupled-field simulation of a sphere-plane electrical contact," in *Proceedings of the Fifty-First IEEE Holm Conference on Electrical Contacts*, 2005., 2005: IEEE, pp. 224-231.
- [118] N. Pandey, I. Jain, E. S. Reddy, and N. P. Gulhane, "Experimental Analysis of Electro-Thermal Contact Resistance of Al and Cu Surfaces," in *2018 5th IEEE Uttar Pradesh Section International Conference on Electrical, Electronics and Computer Engineering (UPCON)*, 2018: IEEE, pp. 1-7.
- [119] D. P. Bertsekas, *Constrained optimization and Lagrange multiplier methods*. Academic press, 2014.
- [120] F. H. Milanez, M. M. Yovanovich, and M. B. Mantelli, "Thermal contact conductance at low contact pressures," *Journal of Thermophysics and Heat Transfer*, vol. 18, no. 1, pp. 37-44, 2004.

- [121] K. N. Babu, "Thermal contact resistance: experiments and simulation," 2015.
- [122] W. Ren, Y. Chen, Z. Wang, S. Xue, and X. Zhang, "Electrical contact resistance of coated spherical contacts," *IEEE Transactions on Electron Devices*, vol. 63, no. 11, pp. 4373-4379, 2016.
- [123] W. Ren, H. Zhi, S. Xue, G. Zhai, and J. Song, "Numerical simulation and experimental verification for contact spot temperature and electrical contact resistance of rivet contacts," in *ICEC 2014; The 27th International Conference on Electrical Contacts*, 2014: VDE, pp. 1-5.
- [124] G. Chester and A. Thellung, "The law of Wiedemann and Franz," *Proceedings of the Physical Society*, vol. 77, no. 5, p. 1005, 1961.